Magnetoelectric, dielectric, and magnetic investigations of multiferroic NixCo1–xFe2O4–SryBa1–yNb2O6 composites

Roberto Köferstein, Maria-Sophie Wartmann, Stefan G Ebbinghaus

Materials Research Bulletin 177 (2024) 112860

Contents lists available at ScienceDirect

Materials Research Bulletin

journal homepage: www.elsevier.com/locate/matresbu

Research Papers

Magnetoelectric, dielectric, and magnetic investigations of multiferroic $Ni_xCo_{1-x}Fe_2O_4$−$Sr_yBa_{1-y}Nb_2O_6$ composites

Roberto Köferstein *, Maria-Sophie Wartmann, Stefan G. Ebbinghaus

Institute of Chemistry, Martin Luther University Halle-Wittenberg, Kurt-Mothes-Straße 2, 06120 Halle, Germany

ARTICLE INFO

Keywords:
Composites
Ceramics
Phase transitions
Magnetic properties
Multiferroics

ABSTRACT

Magnetoelectric $(Ni_xCo_{1-x}Fe_2O_4)_{0.3}$−$(Sr_yBa_{1-y}Nb_2O_6)_{0.7}$ composites with a 0–3 connectivity and different cation stoichiometries were synthesized via a classical mixed-oxide method. XRD patterns of all ceramics show reflections of the target phases $Sr_yBa_{1-y}Nb_2O_6$ and $Ni_xCo_{1-x}Fe_2O_4$. The influence of stoichiometry of the ferrimagnetic and ferroelectric phase on the magnetoelectric behavior was studied on composites with composition of $(Ni_xCo_{1-x}Fe_2O_4)_{0.3}$−$(Sr_{0.5}Ba_{0.5}Nb_2O_6)_{0.7}$ and $(NiFe_2O_4)_{0.3}$−$(Sr_yBa_{1-y}Nb_2O_6)_{0.7}$. The magnetic Curie temperature increases with nickel content. However, the saturation magnetizations as well as the Curie temperatures of the composites are always lower than the ones of bulk $Ni_xCo_{1-x}Fe_2O_4$ samples. The maximum magnetoelectric coefficient (α_{ME}) rises with increasing nickel content from 40 ($x = 0$) to 180 μV Oe^{-1} cm^{-1} ($x = 1$) in accordance with the dynamic magnetostriction coefficient. The evolution of α_{ME} of $(NiFe_2O_4)_{0.3}$−$(Sr_yBa_{1-y}Nb_2O_6)_{0.7}$ composites shows an increase with strontium content up to y 0.5. Higher strontium content leads to a significant reducing of α_{ME}.

1. Introduction

Multiferroic materials exhibit two or more ferroic orders. They are of special interest because of their potential applications as e.g. memories, spintronic, sensors, and in biomedical purposes [1,2]. Recently, Zi et al. [3] have reported on a low-frequency communication device based on the magnetoelectric effect. Coupling between ferro-/ferrimagnetism and ferroelectricity results in the co-called magnetoelectric (ME) effect in which the electrical polarization is affected by a magnetic field and vice versa. Most of the single-phase ME compounds (e. g. $TbMn_2O_5$, $BiMnO_3$) show a small ME effect and/or it appears at low temperatures [4,5]. However, Veena et al. [6] have recently reported on large magnetoelectric coupling at room temperature in Sr_2FeNbO_6. On the other hand, composite materials with separate ferro-/ferrimagnetic and ferroelectric phases often show a strong magnetoelectric response at room temperature, which is essential for technical applications [7,8]. Furthermore, in magnetoelectric composite materials, the ME effect can be tuned by changing the stoichiometry of each single phase and by varying the molar ratio between the ferro-/ferrimagnetic and ferroelectric phase [9,10,11,12]. The coupling between those two phases is mediated by their interfaces and the magnetoelectric effect can be understood as a product property between those ferroic orders [13]. The two different phases composite materials can be arranged in e.g. 0–3 (particles surrounded by a matrix), 2–2 (layers), and 1–3 (pillars in a matrix) dimensionalities [14]. Lead-free 0–3 magnetoelectric composites based on $BaTiO_3$ and MFe_2O_4 have been extensively investigated [9,15-22]. In comparison, composites with the relaxor ferroelectric $Sr_yBa_{1-y}Nb_2O_6$ ($0.25 \leq y \leq 0.75$) have been only rarely studied [23–31]. In contrast to composites with $BaTiO_3$, the ferroelectric phase of $Sr_yBa_{1-y}Nb_2O_6$ in composites is stable even after sintering at high temperatures [32–34]. Ferroelectric $Sr_yBa_{1-y}Nb_2O_6$ crystallized in the open tungsten-bronze structure and shows a diffuse phase transition (DPT) between roughly 313−473 K, depending on y [35–39]. The piezoelectric coefficient also depends on the Sr/Ba ratio (y) [40]. The influence of the stoichiometry of the ferroelectric and ferro-/ferrimagnetic phases on the magnetoelectric output is less well studied [41,42].

The aim of this work is to investigate the influence of the cation stoichiometry of the ferrimagnetic and the ferroelectric phases of $(Ni_xCo_{1-x}Fe_2O_4)_{0.3}$−$(Sr_yBa_{1-y}Nb_2O_6)_{0.7}$ composites on the magnetoelectric output. The samples were synthesized by the conventional mixed-oxide method. Phase evolution and microstructure of the composite ceramics were monitored by XRD, SEM, and EDX. The magnetoelectric behavior was investigated depending on H_{DC}, frequency of H_{AC} and composition. The Curie temperatures were determined by

* Corresponding author.
E-mail address: roberto.koeferstein@chemie.uni-halle.de (R. Köferstein).

https://doi.org/10.1016/j.materresbull.2024.112860
Received 22 September 2023; Received in revised form 25 March 2024; Accepted 22 April 2024
Available online 23 April 2024

thermomagnetometric measurements. Moreover, the samples were characterized by impedance spectroscopy and magnetic measurements.

2. Experimental

2.1. Material preparation

$(Ni_xCo_{1-x}Fe_2O_4)_{0.3}$–$(Sr_{0.5}Ba_{0.5}Nb_2O_6)_{0.7}$ composites with varying Ni/Co contents x = 0, 0.25, 0.5, 0.75, and 1 (= 20.3 wt% $Ni_xCo_{1-x}Fe_2O_4$) were prepared. Additionally, we also prepared $(NiFe_2O_4)_{0.3}$–$(Sr_yBa_{1-y}Nb_2O_6)_{0.7}$ composites with different Sr/Ba ratios y = 0.3, 0.5, 0.6, and 0.7 (= 19.7 – 20.7 wt% $NiFe_2O_4$).

The composites were synthesized by a classical mixed oxide synthesis as described in our previous paper [31]. The oxides and carbonates were mixed in a planetary mill for 4 h using polyamide jars, ZrO_2-balls, and propan-2-ol. To prepare $Ni_xCo_{1-x}Fe_2O_4$, NiO (Berlin—Chemie, puriss.), Co_2O_3 (Alfa Aesar, 99.7%) and Fe_2O_3 (Alfa Aesar, 99.9%) were mixed in the desired molar ratio. After filtering and drying the mixture was calcined in static air at 1423 K for 2 h (heating rate 10 K min^{-1}). $Sr_yBa_{1-y}Nb_2O_6$ was synthesized by mixing stoichiometric amounts of $BaCO_3$ (Merck, > 98.5%), $SrCO_3$ (Sigma-Aldrich, 99.9%), and Nb_2O_5 (Alpha Aesar, 99.9%) and calcining for 5 h at 1473 K (y = 0.3 and 0.5), 1573 K (y = 0.6), and 1703 K for 30 h (y = 0.7) (heating rate 5 K min^{-1}) to get phase pure powders (Fig. S1, supporting information). Composite powders were prepared by mixing $Ni_xCo_{1-x}Fe_2O_4$ and $Sr_yBa_{1-y}Nb_2O_6$ powders to get the target composition of $(Ni_xCo_{1-x}Fe_2O_4)_{0.3}$–$(Sr_yBa_{1-y}Nb_2O_6)_{0.7}$. The resulting composite powders were mixed with 10 wt% of a saturated aqueous polyvinyl alcohol (PVA) solution as a pressing aid and uniaxially pressed at about 110 MPa into pellets (green density: 3.0 g cm^{-3}). These pellets were placed on a ZrO_2 fibre mat and sintered to ceramic bodies between 1273 and 1473 K (heating-/cooling rate 5 K min^{-1}) with a soaking time of 1 h.

2.2. Characterization

X-ray powder diffraction were carried out on a Bruker D8-Advance diffractometer at room temperature, equipped with a one-dimensional silicon strip detector (LynxEye™) using Cu-K_α radiation and a counting time of 1 s per data point. Scanning electron microscope images were collected with a Phenom ProX SEM in backscattered electron mode (BSE). Thermal analyses were performed with a heating-/cooling rate of 10 K min^{-1} in flowing nitrogen (75 ml min^{-1}) using a TA Instruments TGA 550 thermobalance (weighing precision 0.01 %). To determine the magnet transition temperature (Curie point), a bar magnet was placed underneath the balance [43]. A Quantum Design PPMS9 system was used for magnetic and magnetoelectric measurements. Magnetic hysteresis loops were taken at 300 K with magnetic DC field cycling between ±90 kOe. For magnetoelectric and impedance measurements, ceramic samples were sputtered on both sides with 100 nm thick gold electrodes using a Cressington Sputter Coater 108auto. For magnetoelectric measurements the samples were electrically poled along the thickness direction for 18 h at room temperature applying an electric field of about 7 kV cm^{-1} with a current limit of 0.1 mA. Magnetoelectric measurements were performed using a self-made setup [9] with the magnetic DC field parallel to the electrical polarization and a small AC driving field of about 8 Oe was superimposed collinear to the static field by a solenoid. The in-phase voltage (U_{ME}) was recorded by a lock-in technique. The magnetoelectric coefficient (α_{ME}) was calculated as $\alpha_{ME} = U_{ME}\cdot(H_{AC}\cdot d)^{-1}$ (d = sample thickness). The thickness of the ceramic samples was between 0.95 and 1.02 mm. The magnetoelectric performance was investigated at 300 K in a DC field cycling between ±15 kOe at $\nu(H_{AC})$ = 900 Hz. Frequency-dependent measurements were done at the DC field at which the maximum of α_{ME} was found. An Impedance Analyzer 4192A (Hewlett Packard) was used for impedance measurements.

3. Results and discussion

3.1. $(Ni_xCo_{1-x}Fe_2O_4)_{0.3}$–$(Sr_{0.5}Ba_{0.5}Nb_2O_6)_{0.7}$ composites

After pressing to pellets, the composite powders were sintered in static air at 1373 K for 1 h (heating-/ cooling rate: 5 K min^{-1}). The bulk densities of the black ceramic bodies were calculated from their weight and geometric dimension and the relative bulk densities were related to 5.37 g cm^{-3}, calculated from the single crystal densities of $Sr_{0.5}Ba_{0.5}Nb_2O_6$ and $Ni_xCo_{1-x}Fe_2O_4$ considering their nominal molar fractions [44]. The $(Ni_xCo_{1-x}Fe_2O_4)_{0.3}$–$(Sr_{0.5}Ba_{0.5}Nb_2O_6)_{0.7}$ ceramic bodies reveal an increase in density with increasing cobalt content (Fig. 1), e.g. for x = 1 a relative density of 71(1)% was achieved, whereas composites with x = 0 reached 83(1)%.

Fig. 2 shows the XRD patterns after sintering of compacted $(Ni_xCo_{1-x}Fe_2O_4)_{0.3}$–$(Sr_{0.5}Ba_{0.5}Nb_2O_6)_{0.7}$ composite powders at 1373 K. The composite ceramics reveal reflections of cubic $Ni_xCo_{1-x}Fe_2O_4$ (JCPDS #01–074–2081 [$NiFe_2O_4$], #00–022–1086 [$CoFe_2O_4$]) and tetragonal $Sr_{0.5}Ba_{0.5}Nb_2O_6$ (JCPDS #01–074–6520). Weak reflections at 24.7° and 30.5° indicate the formation of a secondary phase (2 – 4 wt %). According to EDX results and previous investigations [31], this secondary phase can be described as orthorhombic $M_{0.4}Fe_{0.6}Nb_2O_6$ (M = Ni/Co) (JCPDS #01–075–2158/ #01–076–2354) with columbite structure which change to a tetragonal rutile structure [JCPDS #01–077–1290/ #01–076–2355] after sintering at 1423 and 1473 K.

Fig. 3 shows the microstructure of selected composite ceramics. Due to the BSE mode of the SEM images, light grey grains represent $Sr_{0.5}Ba_{0.5}Nb_2O_6$ and the dark ones correspond to $Ni_xCo_{1-x}Fe_2O_4$ and secondary phases, respectively. Representative EDX spectra are shown in Fig. S2 (supporting information) confirming the formation of $Sr_{0.5}Ba_{0.5}Nb_2O_6$ and $Ni_xCo_{1-x}Fe_2O_4$ grains. Measurements on several large grains point to a possible iron doping (< 1 at.%) of the $Sr_{0.5}Ba_{0.5}Nb_2O_6$ phase, whereas traces of Sr and Nb in the $Ni_xCo_{1-x}Fe_2O_4$ spectrum are most likely caused by the large interaction volume of the electron beam compared to the small grain size. The EDX spectra of the secondary phase reveal a composition of about $M_{0.4}Fe_{0.6}Nb_2O_6$ (M = Ni/Co), as aforementioned. The sporadic grains of the secondary phase show an irregular shape up to about 3 μm in all samples. After sintering at 1373 K, the $Ni_xCo_{1-x}Fe_2O_4$ phase forms irregular and pyramidal-/octahedral-like grains with dimensions between 0.5 – 3 μm for x = 1 – 0.75 and 0.8 – 5 μm for x = 0. The $Sr_{0.5}Ba_{0.5}Nb_2O_6$ grains show a globular-/irregular shape between 1 – 6 μm for x = 1 which slightly grows to 1 – 9 μm for x = 0. Besides these globular grains, we also observed the appearance of pillar-like $Sr_{0.5}Ba_{0.5}Nb_2O_6$ grains in samples with cobalt-substituted $NiFe_2O_4$. The pillars have dimensions of about 3 – 8×1.5 – 3 μm and the fraction of the pillars moderately increases with increasing cobalt substitution in $Ni_xCo_{1-x}Fe_2O_4$. The formation of pillar-

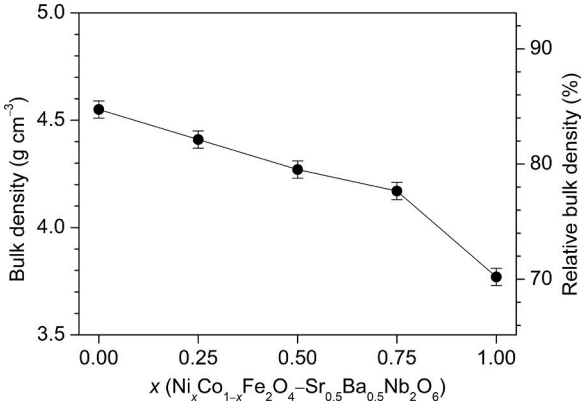

Fig. 1. Bulk densities of $(Ni_xCo_{1-x}Fe_2O_4)_{0.3}$–$(Sr_{0.5}Ba_{0.5}Nb_2O_6)_{0.7}$ composite ceramic bodies after firing at 1373 K for 1 h (heating-/cooling rate 5 K min^{-1}).

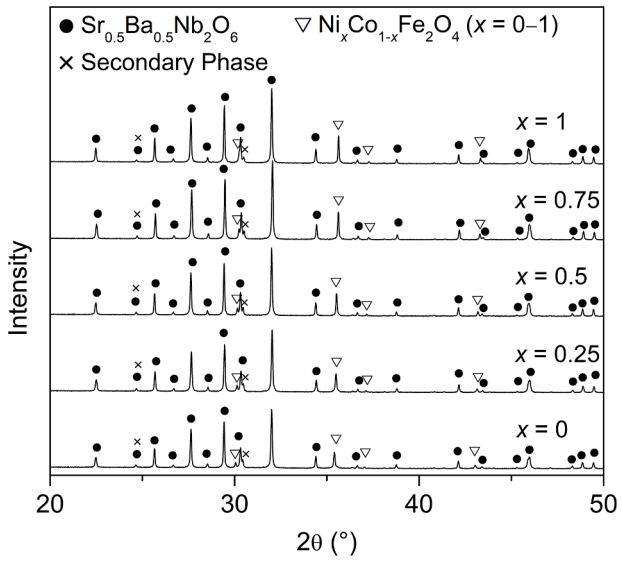

Fig. 2. Room-temperature XRD patterns of $(Ni_xCo_{1-x}Fe_2O_4)_{0.3}$–$(Sr_{0.5}Ba_{0.5}Nb_2O_6)_{0.7}$ powdered composite ceramics after sintering at 1373 K for 1 h (heating-/cooling rate 5 K min^{-1}).

like grains was also observed in pure $Sr_{0.5}Ba_{0.5}Nb_2O_6$ ceramics sintered at high temperatures [45].

3.1.1. Magnetic and dielectric behavior

Fig. 4 shows the field-dependent magnetization curves at 300 K of $(Ni_xCo_{1-x}Fe_2O_4)_{0.3}$–$(Sr_{0.5}Ba_{0.5}Nb_2O_6)_{0.7}$ ceramics sintered at 1373 K. Data have been normalized with respect to the nominal $Ni_xCo_{1-x}Fe_2O_4$ fraction. Magnetization data with respect to the sample mass are shown in Fig. S3 (supporting information). The occurrence of hystereses is due the ferrimagnetic properties of the $Ni_xCo_{1-x}Fe_2O_4$ phase. The coercivity values (inset in Fig. 4) increase with cobalt content from 29 to 260 Oe, because of the higher magnetocrystalline anisotropy constant of Co^{2+} compared to Ni^{2+} [46–48]. The saturation magnetizations (M_s) were calculated by extrapolating the magnetization at high fields to H = 0 because of the presence of small amounts of paramagnetic secondary phases ($M_{0.4}Fe_{0.6}Nb_2O_6$ (M = Ni/Co)) [33,49,50]. As expected, the saturation magnetization at 300 K of the composite ceramics raises with decreasing x from 46.1(2) to 76.7(3) emu g^{-1} (1.93(1) − 3.22(1) μ_B f. u.$^{-1}$) (Fig. 5).

The increase of M_s with cobalt substitution is not only due to different magnetic moments of Ni^{2+} (2 μ_B) and Co^{2+} (3 μ_B), but it also reflects that $NiFe_2O_4$ is an inverse spinel, whereas $CoFe_2O_4$ crystallized in a partly inverse spinel structure [51]. However, the M_s values of the composites are slightly lower than the values of 49.7(2) − 89.4(2) emu g^{-1} (2.09(1) − 3.76(1) μ_B f.u.$^{-1}$) for pure bulk $Ni_xCo_{1-x}Fe_2O_4$ samples, which also increases with Co^{2+} content. The slightly lower M_s values of the composites are caused by the formation of the aforementioned secondary phases primarily leading to cation vacancies in the ferrite grains (Fe/M ≠ 2, M = Ni, Co) and to a small reduction of the $Ni_xCo_{1-x}Fe_2O_4$ amount in the composites. In generally, the development of the saturation magnetization of spinel ferrites with Fe/M ≠ 2, compared to stoichiometric ferrites, is affected by the change of the inversions parameter (rearrangement of the metal cation over the tetragonal and octahedral sites) [52] and the weakening of the superexchange interaction is due the formation of metal vacancies and resulting oxygen vacancies. To investigate this effect, we prepared MFe_2O_4 (M = Ni/Co) ceramics with different Fe/M ratios from 1.90 to 2.22. Fig. S4 (supporting information) shows their evolution of the saturation magnetization. A ratio higher than 2 leads to smaller M_s values for $CoFe_2O_4$ samples, whereas for $NiFe_2O_4$ a slight increase can be obtained, in accordance with investigations by Shafer [53]. In contrast samples with

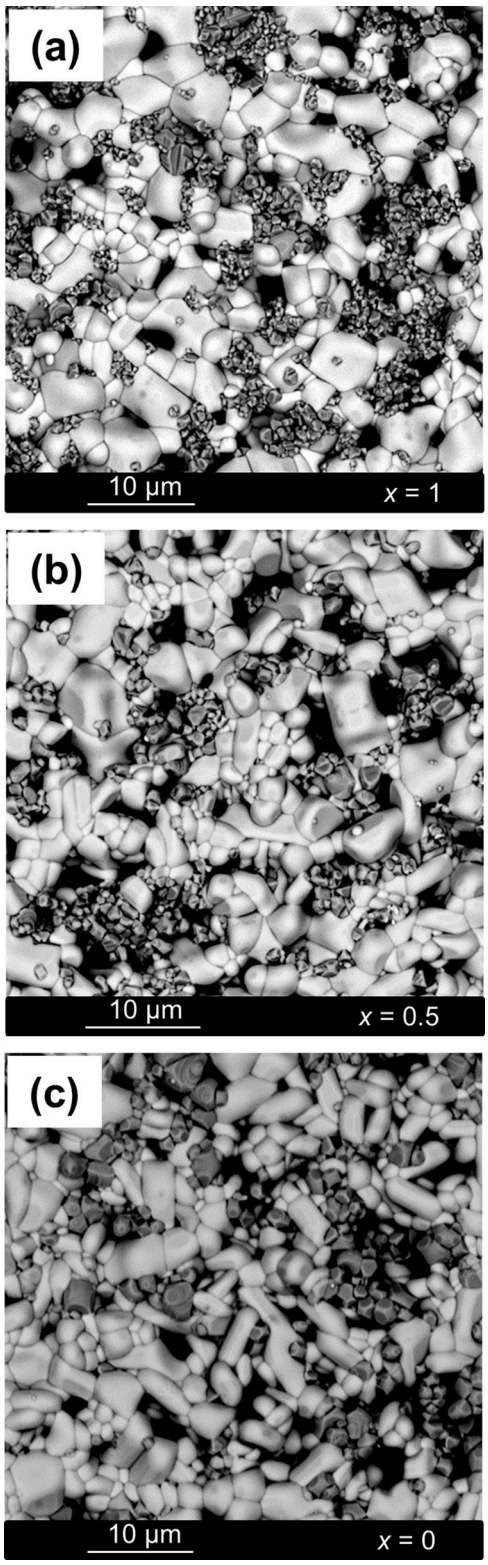

Fig. 3. SEM-BSE images of selected $(Ni_xCo_{1-x}Fe_2O_4)_{0.3}$–$(Sr_{0.5}Ba_{0.5}Nb_2O_6)_{0.7}$ ceramic bodies sintered at 1373 K for 1 h. a) x = 1, b) x = 0.5, c) x = 0.

a Fe/M ratio lower than 2 show lower M_s values in both cases [54]. This effect is more pronounced for $CoFe_2O_4$ samples and reflects the M_s development between the composites and pure $Ni_xCo_{1-x}Fe_2O_4$ ceramics (Fig. 5). These findings suggest an iron deficiency (Fe/M < 2) of the ferrite phase in the composites.

Not only the saturation magnetization but also the Curie

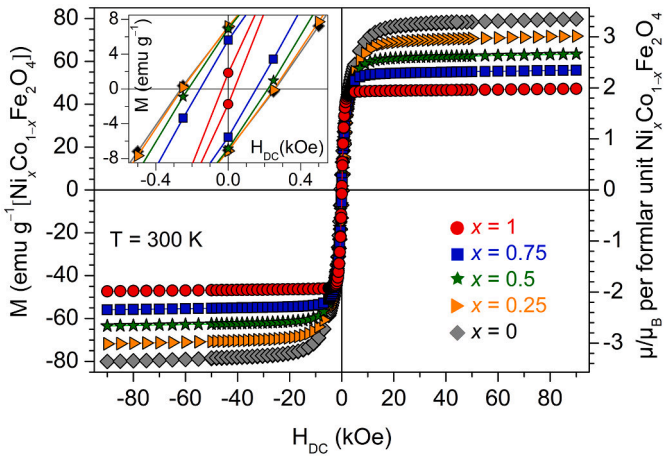

Fig. 4. Magnetization at 300 K for $(Ni_xCo_{1-x}Fe_2O_4)_{0.3}$–$(Sr_{0.5}Ba_{0.5}Nb_2O_6)_{0.7}$ composite ceramics sintered at 1373 K for 1 h. The inset shows M versus H in a small field range. The magnetization values are given with respect to the nominal $Ni_xCo_{1-x}Fe_2O_4$ content.

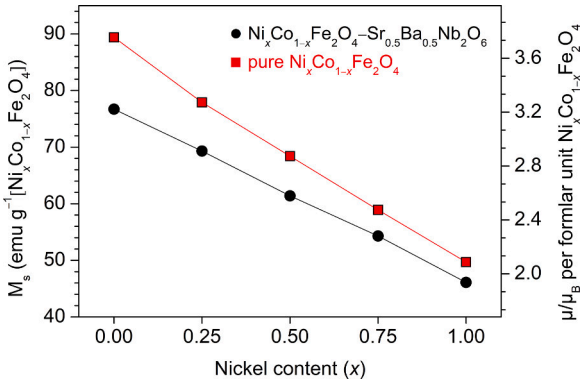

Fig. 5. Dependence of M_s on the nickel content (x) of $(Ni_xCo_{1-x}Fe_2O_4)_{0.3}$–$(Sr_{0.5}Ba_{0.5}Nb_2O_6)_{0.7}$ composites and $Ni_xCo_{1-x}Fe_2O_4$ ceramic samples sintered at 1373 K for 1 h.

temperatures of spinel ferrites strongly depend on their composition. The development of the Curie temperature (T_c) (paramagnetic ⇆ ferrimagnetic transition) of the $Ni_xCo_{1-x}Fe_2O_4$ phase in the composites sintered at 1373 K was measured in a thermobalance in which a magnet was placed underneath the furnace. In the ferrimagnetic state of the sample the magnet applied an extra attractive force on the hanging sample, resulting in an apparently higher weight. During cooling from the paramagnetic to the ferrimagnetic state a sudden rising weight can be observed at T_c (see inset in Fig. 6) [30]. The Curie temperature was determined from the onset of this weight increase. As shown in Fig. 6, T_C increases almost linearly with increasing nickel substitution (x) from 773(1) for $CoFe_2O_4$ to 860(1) K for $NiFe_2O_4$ in the composite ceramics. The Curie temperatures of Co- and Ni-ferrites are in good agreement with literature data [55,56]. According to the two sub-lattice model by Néel, the Curie temperature in spinels is mainly determined by the superexchange interaction (via an O^{2-} ion) between the A and B sub-lattices, representing the cations on the tetrahedral (A) and octahedral (B) sites, respectively [57,58]. A weakening of the strength of the $A-B$ exchange interaction results in a lower Curie temperature. The reported value for the exchange integral $|J_{AB}|$ for $NiFe_2O_4$ (−27.4 K) is higher than for $CoFe_2O_4$ (−22.7 K) [59,60], meaning that the $A-B$ interaction is lower in $CoFe_2O_4$. The weakening of the $A-B$ interaction in $CoFe_2O_4$ is due to a change of the cation distribution between the A and B sites. $NiFe_2O_4$ is a complete inverse spinel, whereas $CoFe_2O_4$ crystallized in a partly invers structure [61]. Additionally, the larger

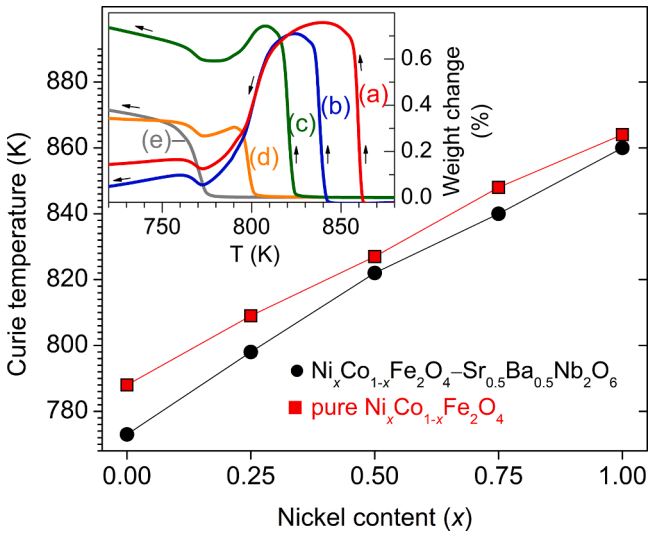

Fig. 6. Evolution of the Curie temperature depending on the nickel content (x) of $(Ni_xCo_{1-x}Fe_2O_4)_{0.3}$–$(Sr_{0.5}Ba_{0.5}Nb_2O_6)_{0.7}$ composites and pure $Ni_xCo_{1-x}Fe_2O_4$ ceramic samples sintered at 1373 K for 1 h. The inset shows the thermogravimetric measurements in flowing nitrogen (cooling rate 10 K min^{-1}) of $(Ni_xCo_{1-x}Fe_2O_4)_{0.3}$–$(Sr_{0.5}Ba_{0.5}Nb_2O_6)_{0.7}$ composite bodies in a magnetic field. x = 1 (a), 0.75 (b), 0.5 (c), 0.25 (d), 0 (e).

cation radius of Co^{2+} and thus an increase in the cubic lattice parameter for cobalt ferrite leads to larger interatomic distances, which also cause a reduction of the $A-B$ exchange interaction strength [57,62,63].

It can further be seen that the Curie temperature of the ferrite phase in the composites is slightly lower than T_C for pure $Ni_xCo_{1-x}Fe_2O_4$ ceramics sintered under the same conditions, which was also observed by Ciomaga et al. [64]. This effect increases slightly with raising Co-substitution. As mentioned above, EDX analysis of the ferrite grains did not show any significant doping. Thus, we suppose that the slightly lower Curie temperatures can be explained by the formation of the secondary phase ($M_{0.4}Fe_{0.6}Nb_2O_6$) and the a small migration of iron into the $Sr_{0.5}Ba_{0.5}Nb_2O_6$ grains in the composite ceramics which causes cation vacancies in the ferrite grains. Cation vacancies influence the cation distribution over the tetrahedral and octahedral sites and the strength of the $A-B$ exchange interaction [54,65]. The Curie temperatures and the XRD patterns of the above-mentioned single phase $NiFe_2O_4$ and $CoFe_2O_4$ ceramics, sintered at 1373 K for 1 h, with different Fe/M ratios (1.90–2.22, M = Ni, Co) are shown in Fig. S5 and S6 (supporting information). It can be seen that a Fe/M ratio lower than 2 leads to a decreasing Curie temperature by 17(2) K for Fe/M = 1.90 in cobalt ferrite, whereas in nickel ferrite the Curie point does not significantly change. On the other hand, a Fe/M ratio higher than 2 causes an increase of T_C by 16(2) and 5(2) K (Fe/M = 2.22) for cobalt ferrite and nickel ferrite, respectively. These findings suggest that the ferrite phase in the composites exhibit an iron deficiency (Fe/M ratio < 2) which leads to slightly lower Curie temperatures of the composites compared to pure $Ni_xCo_{1-x}Fe_2O_4$ samples.

Dielectric properties of the composites were investigated by impedance spectroscopy. The temperature dependence of ε_r' and tan δ at a frequency of 1 kHz is shown in Fig. 7. The permittivity values increase with temperature. $Sr_{0.5}Ba_{0.5}Nb_2O_6$ is a relaxor ferroelectric and shows a diffuse phase transition around 373–423 K (Curie-range [45,66]). In contrast to ceramics of pure $Sr_{0.5}Ba_{0.5}Nb_2O_6$, for which a broad maximum of the permittivity occurs (see also Fig. S7, supporting information) no such maximum were found for the composite ceramic samples. However, the permittivity curves reveal a weak shoulder or at least a significant change in the slope at around 373 K, which is more visible by plotting $\varepsilon_r'^{-1}$ vs. temperature (Fig. S8, supporting information) Rising tan δ values at high temperatures (inset in Fig. 7) are most

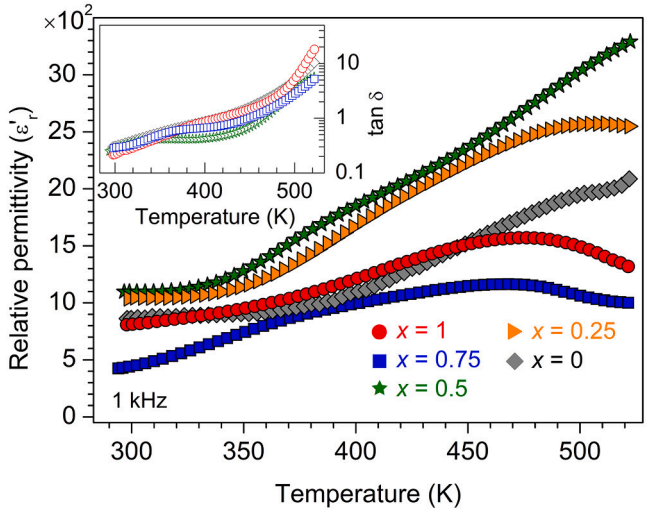

Fig. 7. Dependence of the real part of ε_r' and tan δ (inset) on temperature at 1 kHz for $(Ni_xCo_{1-x}Fe_2O_4)_{0.3}$–$(Sr_{0.5}Ba_{0.5}Nb_2O_6)_{0.7}$ ceramic bodies sintered at 1373 K for 1 h. For the sake of clarity every 4th data point is represented by a symbol.

likely due to a decreasing resistivity of the samples.

Because of the low conductivities of the samples at room temperature ($\sigma_{DC} << 10^{-7}$ S cm^{-1}), the high-temperature impedance data were fitted by an equivalent circuit consisting of one resistance-capacitor (RC) element including a constant phase-shift element. The specific complex impedance (Z^*_{spec}) for a single RC element is described by [67]:

$$Z^*_{spec} = \frac{\rho_{DC}}{1 + (i\omega\tau)^{\beta}} \quad (1)$$

where, β is the constant phase-shift (CPE) coefficient and $\tau = \rho_{DC}\varepsilon\varepsilon_0$. Cole-Cole plots of the specific impedance of the $(Ni_xCo_{1-x}Fe_2O_4)_{0.3}$–$(Sr_{0.5}Ba_{0.5}Nb_2O_6)_{0.7}$ magnetoelectric composites can be well described by one RC element (inset in Fig. 8). The calculated specific DC resistivities (ρ_{DC}) of the $(Ni_xCo_{1-x}Fe_2O_4)_{0.3}$–$(Sr_{0.5}Ba_{0.5}Nb_2O_6)_{0.7}$ ceramics are similar for all samples. ρ_{DC} decreases slightly with increasing nickel content from 8.30(2)·10^2 kΩcm ($x = 0$) to 5.38 (3)·10^2 kΩcm ($x = 0.75$) and finally rises to 15.56(3)·10^2 kΩcm for $x = 1$ (Fig. 8). Due to the electrically leaky nature of ferrites, the DC resistivities of the composites are significantly lower compared to pure $Sr_{0.5}Ba_{0.5}Nb_2O_6$ (83.71(7)·10^2 kΩcm).

3.1.2. *Magnetoelectric properties*

The magnetoelectric coefficient (α_{ME}) dependence on the static magnetic field (H_{DC}) at 300 K for $(Ni_xCo_{1-x}Fe_2O_4)_{0.3}$–$(Sr_{0.5}Ba_{0.5}Nb_2O_6)_{0.7}$ composite ceramics sintered at 1373 K is shown in Fig. 9. The evolution of α_{ME} reveals a hysteretic behavior with coercive fields smaller than 100 Oe. α_{ME} increases with rising H_{DC} field up to a maximum/minimum (α_{MEmax}) and then continuously decreases to zero at higher fields.

As seen in Fig. 10, α_{MEmax} growths with increasing nickel content from 40(2) μV cm^{-1} Oe^{-1} ($x = 0$) to 180(10) μV cm^{-1} Oe^{-1} ($x = 1$). Analogous tendencies were also reported in magnetoelectric composites consisting of Ni/Co-ferrites and $BaTiO_3$, $Pb(Zr/Ti)O_3$, or $PbFe_{0.5}Nb_{0.5}O_3$ [41,68,69,70]. The value of the magnetoelectric coefficient is influenced by resistivity, density, and grain size of the ceramics, as well as by the magnetostrictive-/ piezoelectric output of the individual composite phases. In generally, considerably decreasing resistivities (at least one order of magnitude) of the samples can reduced the magnetoelectric effect [30,31,71,72]. However, the resistivity values of the samples are in the same order of magnitude and also the grain sizes are in a comparable range. The density of the ceramics decreases with nickel substitution, but this would rather degrade the magnetoelectric coupling. Therefore, we conclude that the magnetoelectric output of the samples is mainly determined by the magnetostrictive behaviour of the $Ni_xCo_{1-x}Fe_2O_4$ phase. On the other hand, the magnetostriction induced by a static magnetic field (H_{DC}) is reduced from $CoFe_2O_4$ to $NiFe_2O_4$ which would expected lower α_{ME} values for composite samples with increasing nickel content [73,74]. However, to measure the magnetoelectric performance, an alternating magnetic field (H_{AC}) is superimposed to the H_{DC} field. As pointed out by Aubert et al. [70,75], the applied H_{AC} field leads to a dynamic deformation (piezomagnetic effect) of the ferrite grains. The resulting dynamic magnetostriction coefficient of $CoFe_2O_4$ is lower than the one of $NiFe_2O_4$ for low H_{AC} fields [70,75], which explains the observed α_{ME} evolution of our $(Ni_xCo_{1-x}Fe_2O_4)_{0.3}$–$(Sr_{0.5}Ba_{0.5}Nb_2O_6)_{0.7}$ composites. Higher α_{ME} values for composites with $NiFe_2O_4$ compared to $CoFe_2O_4$ were also found for other sintering temperatures (Fig. 11). The $NiFe_2O_4$ based composites always show higher α_{ME} values, although the density of the $CoFe_2O_4$–$Sr_{0.5}Ba_{0.5}Nb_2O_6$ ceramics is higher which should lead to a better connectivity between the ferroelectric and ferromagnetic grains. After sintering at 1473 K in both composite

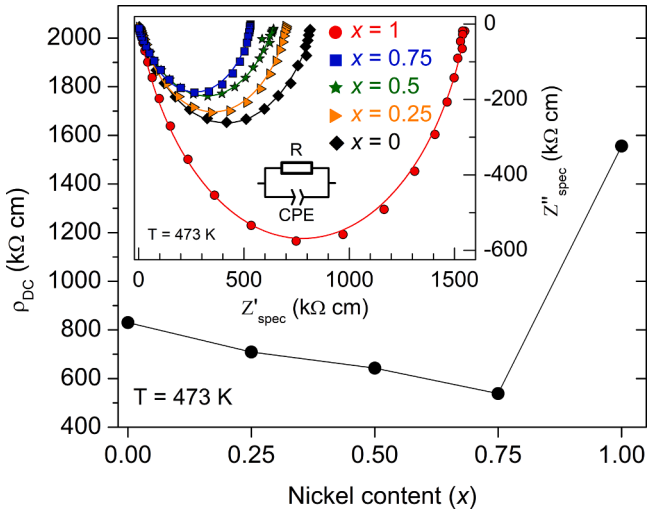

Fig. 8. Development of the specific DC resistivity with composition of $(Ni_xCo_{1-x}Fe_2O_4)_{0.3}$–$(Sr_{0.5}Ba_{0.5}Nb_2O_6)_{0.7}$ ceramic sintered at 1373 K for 1 h. The uncertainties of the data are smaller than the symbol size. The inset shows the Cole-Cole plots of the samples.

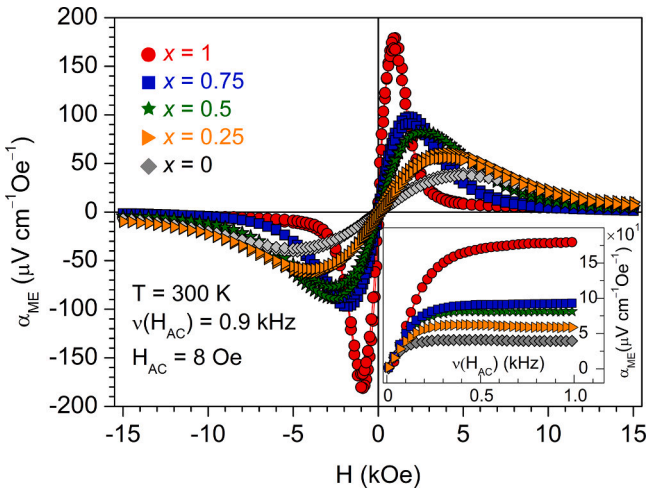

Fig. 9. Magnetoelectric coefficient (α_{ME}) vs. magnetic DC field for $(Ni_xCo_{1-x}Fe_2O_4)_{0.3}$–$(Sr_{0.5}Ba_{0.5}Nb_2O_6)_{0.7}$ composites sintered at 1373 K for 1 h. The inset shows the frequency dependence (H_{AC}) of α_{ME} at $H_{DC(\alpha_{max})}$. For the sake of clarity, in the inset every 10th data point is represented by a symbol.

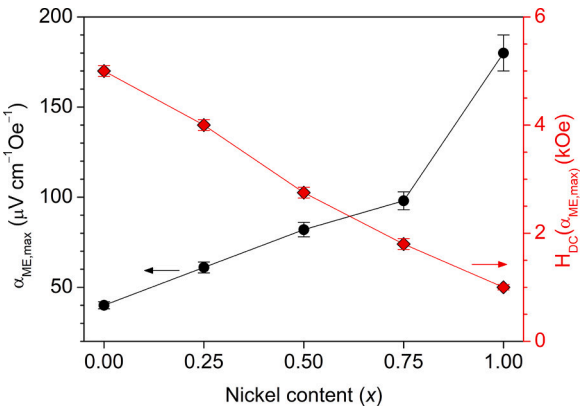

Fig. 10. Maximum of the magnetoelectric coefficient ($\alpha_{ME,max}$) and the H_{DC} field at which the maximum of α_{ME} appeared ($H_{DC(\alpha_{max})}$) depending on the composition x for $(Ni_xCo_{1-x}Fe_2O_4)_{0.3}$–$(Sr_{0.5}Ba_{0.5}Nb_2O_6)_{0.7}$.

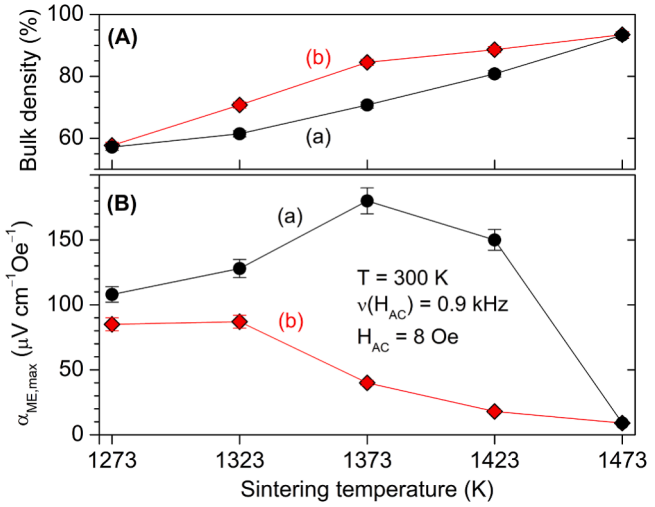

Fig. 11. Relative bulk density (**A**) and maximum magnetoelectric coefficient ($\alpha_{ME,max}$) (**B**) of $(NiFe_2O_4)_{0.3}$–$(Sr_{0.5}Ba_{0.5}Nb_2O_6)_{0.7}$ (a) and $(CoFe_2O_4)_{0.3}$–$(Sr_{0.5}Ba_{0.5}Nb_2O_6)_{0.7}$ (b) composites versus sintering temperature (soaking time 1 h, heating-/cooling rate 5 K min^{-1}). The uncertainties of the data are sometimes smaller than the symbol size.

samples α_{ME} drops down because of a considerable increase in conductivity of more than one order of magnitude [31].

The H_{DC} field at which α_{ME} reaches its maximum ($H_{DC(\alpha_{max})}$) almost linearity decreases with x from 5.0 to 1.0 kOe (Fig. 10) as a result of the change in the magnetostrictive behaviour of $Ni_xCo_{1-x}Fe_2O_4$. The magnetoelectric effect in composites is widely accepted as a product property between a magnetostrictive ($Ni_xCo_{1-x}Fe_2O_4$) and a piezoelectric material ($Sr_{0.5}Ba_{0.5}Nb_2O_6$) [76,77]. Therefore, the field-dependence development of the magnetoelectric coefficient reflects the magnetostriction evolution of $Ni_xCo_{1-x}Fe_2O_4$. The maximum slop of the magnetostriction (strain derivative) and the maximum of the piezomagnetic coefficient of $NiFe_2O_4$ appears at a lower H_{DC} field in contrast to $CoFe_2O_4$ [70,75].

3.2. $(NiFe_2O_4)_{0.3}$–$(Sr_yBa_{1-y}Nb_2O_6)_{0.7}$ composites

In a second set of samples with $NiFe_2O_4$ as the ferrimagnetic component, the Sr/Ba ratio of the ferroelectric component was varied and its effect on the dielectric and magnetoelectric properties was studied. The $(NiFe_2O_4)_{0.3}$–$(Sr_yBa_{1-y}Nb_2O_6)_{0.7}$ composites with $y = 0.3$, 0.5, 0.6, and 0.7 were sintered at 1373 K for 1 h and reached relative densities of 71(1) −72(1)% ($y = 0.5$, 0.6, 0.7) and 76(1)% ($y = 0.3$), respectively. The relative densities were related to 5.30−5.39 g cm^{-3}, depending on y [44] (see Tab. S1, supporting information). Up to a sintering temperature of 1373 K, the XRD patterns (Fig. S9, supporting information) show reflections of $Sr_yBa_{1-y}Nb_2O_6$, $NiFe_2O_4$ and small amounts (2 − 4 wt%) of orthorhombic or tetragonal $(NiFe)Nb_2O_6$ [JCPDS #01–077–1290/ #01–076–2355] as secondary phase [31], as aforementioned. Additionally, for the sintered composites with $y = 0.7$ reflections at 17.6, 22.9, 28.2, 29.1, and 31.8° in the XRD pattern indicate the formation of $SrNb_2O_6$ (JCPDS #01–072–2088) with a fraction of about 20 wt%. Sintering at 1423 K leads in the case of composites with $y = 0.3$ to the formation of small amounts (ca. 6 wt%) of $Ba_3(Fe,Ni)Nb_6O_{21}$ (JCPDS #01–079–0074, #01–079–0075), as confirmed by EDX analysis. The phase composition for $y = 0.5$, 0.6 and 0.7 does not change after firing at 1423 K. However, in all samples, the orthorhombic $(NiFe)Nb_2O_6$ phase completely transforms to the tetragonal one with rutile structure [31] (Fig. S10, supporting information) after sintering above 1373 K.

The saturation magnetization values, related to the nominal $NiFe_2O_4$ content, are between 46.1(2) − 47.0(2) emu g^{-1} for composites sintered at 1373 K and thus independent on the strontium content (y) as expected. The same is true for other sintering temperatures (Fig. S11, supporting information). As mentioned above, these values are slightly lower than the M_s values of pure $NiFe_2O_4$.

The evolution of the permittivity with temperature at 1 kHz depending on the Sr content (y) is depicted in Fig. 12. All samples show increasing permittivity values with rising temperatures and a decrease of ε_r' above 473 K. The permittivity curves of the ceramic bodies do not show a clear maximum reflecting the transition from the ferroelectric to the paraelectric state. In contrast, measurements on phase-pure $Sr_yBa_{1-y}Nb_2O_6$ ceramics show dielectric maxima at 324(2), 353(2), 375(2), and 506(2) K (Fig. S7, supporting information), in accordance with literature data [36,39]. As shown in the inset of Fig. 12, the DC resistivity values, calculated from the impedance data, of the $(NiFe_2O_4)_{0.3}$–$(Sr_yBa_{1-y}Nb_2O_6)_{0.7}$ composites lie in the same order of magnitude. Composites with $y = 0.5$ and 0.6 reveal only slightly lower DC resistivity values than samples with $y = 0.3$ and 0.7.

The maximal magnetoelectric response (α_{MEmax}) of $(NiFe_2O_4)_{0.3}$–$(Sr_yBa_{1-y}Nb_2O_6)_{0.7}$ samples depending on y is shown in Fig. 13. α_{MEmax} rises from $y = 0.3$ to $y = 0.5$ reflecting the increasing piezoelectric coefficient of $Sr_yBa_{1-y}Nb_2O_6$ with rising strontium content (y) [40]. However, the significantly lower α_{MEmax} values for $y = 0.6$ and especially for 0.7 is unexpected. The resistivities of the samples (inset in

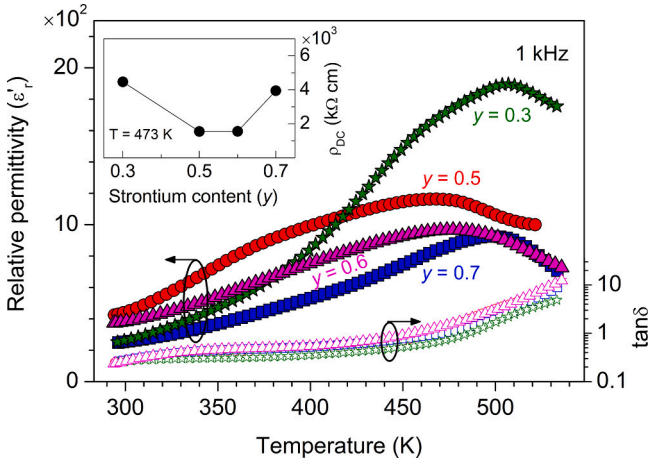

Fig. 12. Dielectric behavior (ε_r'/closed symbols, tan δ/open symbols) at 1 kHz for $(NiFe_2O_4)_{0.3}$–$(Sr_yBa_{1-y}Nb_2O_6)_{0.7}$ ceramic bodies sintered at 1373 K for 1 h. For the sake of clarity every 4th data point is represented by a symbol. The inset shows the specific DC resistivity in dependence of the strontium content (y). The uncertainties of the data are smaller than the symbol size.

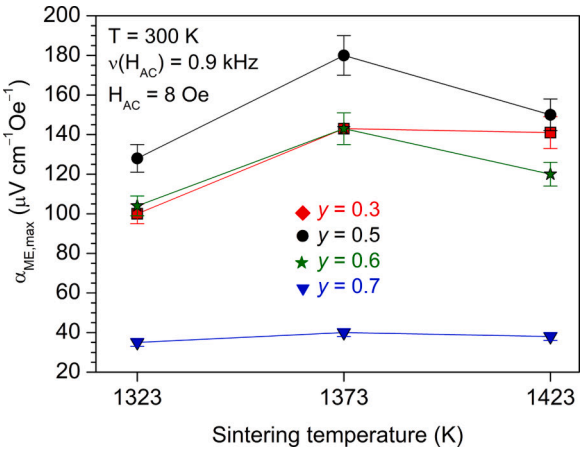

Fig. 13. Maximum magnetoelectric coefficient (α_{ME}) depending on the sintering temperature for $(NiFe_2O_4)_{0.3}$–$(Sr_yBa_{1-y}Nb_2O_6)_{0.7}$ composites.

Fig. 12), which also influenced the magnetoelectric output, differ only slightly from each other (1.6 − 4.5·10^3 kΩcm) and can therefore not explain the reduced α_{MEmax} values for $y > 0.5$. We suppose that the reason for the decline of α_{MEmax} lie in the microstructure and the formation of non-ferroelectric $SrNb_2O_6$ [78] for $y = 0.7$. Due to the higher calcining temperatures necessary for the formation of phase-pure $Sr_yBa_{1-y}Nb_2O_6$ ($y = 0.6$, 0.7) the ferroelectric phase in the resulting composites reveal considerably larger grain sizes. For example, after sintering at 1373 K, the size of the $Sr_yBa_{1-y}Nb_2O_6$ grains are between 1 − 6 μm ($y = 0.3$, 0.5), 1 − 12 μm ($y = 0.6$), and 2 − 33 μm ($y = 0.7$), whereas the size of the $NiFe_2O_4$ grains (0.5 − 3 μm) do not differ significantly with y (Fig. S12, supporting information). We suppose that the large grain size of the ferroelectric phase for $y > 0.5$ leads to a poorer contact between the ferrimagnetic and ferroelectric grains. The strong reduction of α_{ME} for composites with $y = 0.7$ may additionally caused by the formation of considerable amounts of $SrNb_2O_6$ of about 21 vol%, which appears as cuboid-like grains (1 − 4 μm) near the $Sr_{0.7}Ba_{0.3}Nb_2O_6$ grains and hinders an effective mechanical coupling between nickel ferrite and strontium barium niobate grains (Fig. S13, supporting information). The complete development of α_{ME} depending on H_{DC} for all $(NiFe_2O_4)_{0.3}$–$(Sr_yBa_{1-y}Nb_2O_6)_{0.7}$ samples is shown in Fig. S14 (supporting information).

The highest magnetoelectric coefficient was found for $y = 0.5$, whereas $Sr_yBa_{1-y}Nb_2O_6$ with significantly higher strontium content are less suitable as ferroelectric components for 0 − 3 magnetoelectric composite ceramics. Additionally, during the sintering process, composites with a $Sr_yBa_{1-y}Nb_2O_6$ composition near the limit of the ferroelectric range ($y = 0.3$, 0.7), tend to segregate into barium- and strontium-rich phases, respectively.

4. Conclusion

Magnetoelectric $(Ni_xCo_{1-x}Fe_2O_4)_{0.3}$–$(Sr_yBa_{1-y}Nb_2O_6)_{0.7}$ composite ceramics were prepared by the conventional mixed-oxide method. The influence of the nickel content on the magnetoelectric output was investigated on samples containing $Sr_{0.5}Ba_{0.5}Nb_2O_6$ as ferroelectric component. After sintering at 1373 K for 1 h, densities of the ceramics in the range 70−85% were achieved, which slightly decrease with rising nickel content (x). SEM investigations confirm a 0–3 connectivity of the samples with $Ni_xCo_{1-x}Fe_2O_4$ grains up to 5 μm and $Sr_{0.5}Ba_{0.5}Nb_2O_6$ grains up to 9 μm. DC conductivities of the ceramic samples differs only slightly with x. The magnetoelectric coefficient (α_{ME}) shows hystereses with maxima/minima at H_{DC} between ±1.0 and ±5.0 kOe depending on x. The maximum magnetoelectric coefficient ($\alpha_{ME,max}$) considerably rises with nickel content from 40 to 180 μV Oe^{-1} cm^{-1} (@ 900 Hz). The development of $\alpha_{ME,max}$ with x is similar to the evolution of the dynamic magnetostriction of the ferrite phase. The magnetic Curie temperature also increases with nickel content, however the Curie temperatures of the $(Ni_xCo_{1-x}Fe_2O_4)_{0.3}$–$(Sr_{0.5}Ba_{0.5}Nb_2O_6)_{0.7}$ composites are lower than for pure $Ni_xCo_{1-x}Fe_2O_4$ ceramics most likely because of cation vacancies in the ferrite phase. The influence of the Sr/Ba ratio in the ferroelectric phase was investigated on $(NiFe_2O_4)_{0.3}$–$(Sr_yBa_{1-y}Nb_2O_6)_{0.7}$ ceramic specimens. $\alpha_{ME,max}$ increases with the strontium content, however for $y \gg 0.5$ $\alpha_{ME,max}$ considerably decreases due to the formation of a larger amount of secondary phases and/or large grain sizes of $Sr_yBa_{1-y}Nb_2O_6$ ($y > 0.5$) which hinders an effective coupling between the ferrimagnetic and ferroelectric phase.

The investigations show that the magnetoelectric performance of the system $(Ni_xCo_{1-x}Fe_2O_4)$–$(Sr_yBa_{1-y}Nb_2O_6)$ is influenced by the stoichiometries of both composite phases. Additionally, the study emphasized the importance of the dynamic magnetostriction for the magnetoelectric output.

CRediT authorship contribution statement

Roberto Köferstein: Writing – review & editing, Writing – original draft, Validation, Project administration, Methodology, Investigation, Formal analysis, Conceptualization. **Maria-Sophie Wartmann:** Validation, Investigation. **Stefan G. Ebbinghaus:** Writing – review & editing, Validation, Supervision, Resources.

Declaration of competing interest

The authors declare that they have no known competing financial interests or personal relationships that could have appeared to influence the work reported in this paper.

Data availability

Data will be made available on request.

Supplementary materials

Supplementary material associated with this article can be found, in the online version, at doi:10.1016/j.materresbull.2024.112860.

References

[1] C.M. Leung, J. Li, D. Viehland, X. Zhuang, A Review on Applications of Magnetoelectric Composites: From Heterostructural Uncooled Magnetic Sensors, Energy Harvesters to Highly Efficient Power Converters, J. Phys. D Appl. Phys. 51 (2018) 263002.
[2] T.R. Nizamov, A.A. Amirov, T.O. Kuznetsova, I.V. Dorofievich, I.G. Bordyuzhin, D. G. Zhukov, A.V. Ivanova, A.N. Gabashvili, N. Yu. Tabachkova, A.A. Tepanov, I. V. Shchetinin, M.A. Abakumov, A.G. Savchenko, A.G. Majouga, Synthesis and Functional Characterization of $Co_xFe_{3-x}O_4$-$BaTiO_3$ Magnetoelectric Nanocomposites for Biomedical Applications, Nanomater 13 (2023) 811.
[3] G. Zi, Z. Ma, Y. Wang, Y. Wang, Z. Jia, S. Zhao, D. Huang, T. Wang, Miniaturized Low-Frequency Communication System Based on the Magnetoelectric Effect, Micromachines 14 (2023) 1830.
[4] P.R. Mickel, H. Jeen, P. Kumar, A. Biswas, A.F. Hebard, Proximate Transition Temperatures Amplify Linear Magnetoelectric Coupling in Strain-Disordered Multiferroic BiMnO3, Phys. Rev. B 93 (2016) 134205.
[5] N. Hur, S. Park, P.A. Sharma, J.S. Ahn, Guha S, S.W. Cheong, Electric Polarization Reversal and Memory in a Multiferroic Material Induced by Magnetic Fields, Nature 429 (2004) 392–395.
[6] V.S. Veena, R. Revathy, A.A. Kumar Nair, M.T. Rahul, N. Kalarikkal, M.M. Devi, A. Anand, R.K. Veena, S. Sagar, Room Temperature Magnetoelectric Effect in Sr_2FeNbO_6 Perovskite: A Theory Supported Experimental Investigation, J. Solid State Chem. 327 (2023) 124286.
[7] J.M. Caicedo, J.A. Zapata, M.E. Gómez, P. Prieto, Magnetoelectric Coefficient in $BiFeO_3$ Compounds, J. Appl. Phys. 103 (2008) 07E306.
[8] J. Ma, J. Hu, Z. Li, C.W. Nan, Recent Progress in Multiferroic Magnetoelectric Composites: From Bulk to Thin Films, Adv. Mater. 23 (2011) 1062–1087.
[9] T. Walther, U. Straube, R. Köferstein, S.G. Ebbinghaus, Hysteretic Magnetoelectric Behavior of $CoFe_2O_4$–$BaTiO_3$ Composites Prepared by Reductive Sintering and Reoxidation, J. Mater. Chem. C 4 (2016) 4792–4799.

[10] T. Walther, U. Straube, R. Köferstein, S.G. Ebbinghaus, Novel Magnetoelectric Composites of Cobalt Iron Alloy and Barium Titanate, J. Am. Ceram. Soc. 100 (2017) 1502–1507.

[11] I.V. Lisnevskaya, I.A. Aleksandrova, Gel Synthesis of Hexaferrites $Pb_{1-x}La_xFe_{12-x}ZnxO_{19}$ and Properties of Multiferroic Composite Ceramics PZT–$Pb_{1-x}La_xFe_{12-x}ZnxO_{19}$, Nanomaterials 10 (2020) 1630.

[12] R.Goel Vandana, A.K.Singh Shashikant, S. Kumar, Response of DC Biased Magnetoelectric Coupling in 0–3 Type Particulate Lanthanum Modified PZT-CFO Composites, Mater. Today Commun. 37 (2023) 106985.

[13] J. van Suchtelen, Product Properties: A New Application of Composite Materials, Phillips Res. Repts. 27 (1972) 28–37.

[14] R.E. Newnham, D.P. Skinner, L.E. Cross, Connectivity and Piezoelectric-Pyroelectric Composites, Mat. Res. Bull. 13 (1978) 525–536.

[15] J. van den Boomgaard, R.A.J. Born, A Sintered Magnetoelectric Composite Material $BaTiO_3$-Ni(Co,Mn)Fe_2O_4, J. Mater. Sci. 13 (1978) 1538–1548.

[16] R. Gao, Z. Wang, G. Chen, X. Deng, W. Cai, C. Fu, Influence of Core Size on the Multiferroic Properties of $CoFe_2O_4$@$BaTiO_3$ Core Shell Structured Composites, Ceram. Int. 44 (2018) S84–S87.

[17] T. Ramesh, V. Rajendar, S.R. Murthy, $CoFe_2O_4$–$BaTiO_3$ Multiferroic Composites: Role of Ferrite and Ferroelectric Phases on the Structural, Magneto Dielectric Properties, J. Mater. Sci.: Mater. Electron. 28 (2017) 11779–11788.

[18] G. Schileo, Recent Developments in Ceramic Multiferroic Composites Based on Core/Shell and other Heterostructures Obtained by Sole-Gel Routes, Prog. Solid State Chem. 41 (2013) 87–98.

[19] J. Ryu, S. Priya, K. Uchino, H.E. Kim, Magnetoelectric Effect in Composites of Magnetostrictive and Piezoelectric Materials, J. Electroceram. 8 (2002) 107119.

[20] D. Padmapriya, D. Dhayanithi, M.T. Rahul, N. Kalarikkal, N.V. Giridharan, Study of Room-Temperature Magnetoelectric Coupling in (1-x)$BaTiO_3$ and (x)$NiFe_2O_4$ Multiferroic Composites, Appl. Phys. A 127 (2021) 293.

[21] S. Ahmed, M. Atif, A.U. Rehman, S. Bashir, N. Iqbal, W. Khalid, Z. Ali, M. Nadeem, Enhancement in the Magnetoelectric and Energy Storage Properties of Core-Shell-like $CoFe_2O_4$-$BaTiO_3$ Multiferroic Nanocomposite, J. Alloys Compd. 883 (2021) 160875.

[22] A. Sasmal, J. Arout Chelvane, A. Arockiarajan, Development of a Novel Lead Free ($CoFe_{1.9}Bi_{0.1}O_4$/$BaTi_{0.89}Sn_{0.11}O_3$/$CoFe_{1.9}Bi_{0.1}O_4$) Magnetoelectric Composite via New Design Strategy, J. Alloys Compd. 960 (2023) 170733.

[23] S. Tiwari, S. Vitta, Magnetoelectric and Magnetodielectric Coupling and Microwave Resonator Characteristics of $Ba_{0.5}Sr_{0.5}Nb_2O_6$/$CoCr_{0.4}Fe_{1.6}O_4$ Multiferroic Composite, Sci. Rep. 8 (2018) 11619.

[24] X.M. Chen, Y.H. Tang, I.W. Chen, Z.C. Xu, S.Y. Wu, Dielectric and Magnetoelectric Characterization of $CoFe_2O_4$/$Sr_{0.5}Ba_{0.5}Nb_2O_6$ Composites, J. Appl. Phys. 96 (2004) 6520–6522.

[25] S.R. Jigajeni, S.V. Kulkarni, Y.D. Kolekar, S.B. Kulkarni, P.B. Joshi, $Co_{0.7}Mg_{0.3}Fe_{2-x}Mn_xO_4$–$Sr_{0.5}Ba_{0.5}Nb_2O_6$ Magnetoelectric Composites, J. Alloys Compd. 492 (2010) 402–405.

[26] M.M. Sutar, S.R. Kokare, S.H. Kshirsagar, D.J. Salunkhe, P.B. Joshi, Synthesis and Magnetoelectric Studies on BSN-CNFM ME Composites, AIP Conf. Proc 1372 (2011) 220–225.

[27] Y.H. Tang, X.M. Chen, Y.J. Li, X.H. Zheng, Dielectric and Magnetoelectric Characterization of $CoFe_2O_4$/$Ba_{0.5}5Sr_{0.25}Ca_{0.2}Nb_2O_6$ Composites, Mater. Sci. Eng. B 116 (2005) 150–155.

[28] S.R. Jigajeni, A.N. Tarale, D.J. Salunkhe, S.B. Kulkarni, P.B. Joshi, Magnetoelectric and Magnetodielectric Properties of SBN–CMFO Nanocomposites, Appl. Nanosci. 2 (2012) 275–283.

[29] S.S. Rathore, S. Vitta, Large Low Field Room Temperature Magneto-Dielectric Response from $(Sr_{0.5}Ba_{0.5})Nb_2O_6$/$Co(Cr_{0.4}Fe_{1.6})O_4$ Bulk 3-0 Composites, Mater. Sci. Eng. B 204 (2016) 1–7.

[30] R. Köferstein, F. Oehler, S.G. Ebbinghaus, Fine-grained Magnetoelectric $Sr_{0.5}Ba_{0.5}Nb_2O_6$−$CoFe_2O_4$ Composites Synthesized by a Straightforward One-Pot Method, Mater. Chem. Phys. 278 (2022) 125616.

[31] R. Köferstein, S.G. Ebbinghaus, Improvement of the Magnetoelectric Response in $NiFe_2O_4$-$Sr_{0.5}Ba_{0.5}Nb_2O_6$ Composites using $LiNbO_3$ as Sintering Additive, J. Eur. Ceram. Soc. 43 (2023) 6137–6144.

[32] K. Kamishima, Y. Nagashima, K. Kakizaki, N. Hiratsuka, K. Watanabe, T. Mise, H. Naganuma, S. Okamura, Simple Process Synthesis of $BaTiO_3$–(Ni,Zn,Cu)Fe_2O_4 Ceramic Composite, J. Phys. Soc. Jpn. 77 (2008) 064801.

[33] R. Köferstein, T. Walther, D. Hesse, S.G. Ebbinghaus, Fine-grained $BaTiO_3$–$MgFe_2O_4$ Composites Prepared by a Pechini-like Process, J. Alloys Compd. 638 (2015) 141–147.

[34] Y.J. Li, X.M. Chen, Y.Q. Lin, Y.H. Tang, Magnetoelectric effect of $Ni_{0.8}Zn_{0.2}Fe_2O_4$/$Sr_{0.5}Ba_{0.5}Nb_2O_6$ composites, J. Eur. Ceram. Soc. 26 (2006) 2839–2844.

[35] P.B. Jamieson, S.C. Abrahams, J.L. Bernstein, Ferroelectric Tungsten Bronze-Type Crystal Structures. I. Barium Strontium Niobate $Ba_{0.27}Sr_{0.75}Nb_2O_{5.78}$, J. Chem. Phys. 48 (1968) 5048–5057.

[36] A.M. Glass, Investigation of the Electrical Properties of $Sr_{1-x}Ba_xNb_2O_6$ with Special Reference to Pyroelectric Detection, J. Appl. Phys 40 (1969) 4699–4713.

[37] T. Lukasiewicz, M.A. Swirkowicz, J. Dec, W. Hofman, W. Szyrski, Strontium-Barium Niobate Single Crystal Growth and Ferroelectric Properties, J. Cryst. Growth 310 (2008) 1464–1469.

[38] R.R. Neurgainkar, W.K. Cory, Progress in Photorefractive Tungsten Bronze Crystals, J. Opt. Soc. Am. B 3 (1986) 274–282.

[39] M. Said, T.S. Velayuthamn, W.C. Gan, W.H. Abd Majid, The Structural and Electrical Properties of $Sr_xBa_{(1-x)}Nb_2O_6$ (SBN) Ceramic with Varied Composition, Ceram. Inter. 41 (2015) 7119–7124.

[40] R.R. Neurgaonkar, J.R. Oliver, W.K. Cory, L.E. Cross, D. Viehland, Piezoelectricity in Tungsten Bronze Crystals, Ferroelectrics 160 (1994) 265–276.

[41] M.J. Fesharaki, H. Ahmadvand, Structural, Dielectric, Magnetic and Magnetoelectric Properties of the PFN-PT/$Co_{1-x}Ni_xFe_2O_4$ Multiferroic Composites, J. Magn. Magn. Mater. 549 (2022) 169017.

[42] M. Breitenbach, K. Dörr, S.G. Ebbinghaus, Magnetoelectric Properties of $Co_{1-x}Ni_xFe_2O_4$/$BaTiO_3$ Heterostructures with 3–3 Connectivity Obtained by Eutectic Crystallization, Phys. Status Solidi B 257 (2020) 1900618.

[43] S.D. Norem, M.J. O'Neill, A.P. Gray, The Use of Magnetic Transitions in Temperature Calibration and Performance Evaluation of Thermogravimetric Systems, Thermochim. Acta 1 (1970) 29–38.

[44] G.W. Marks, L.A. Monson, Effect of Certain Group IV Oxides on Dielectric Constant and Dissipation Factor of Barium Titanate, Ind. Eng. Chem. 47 (1955) 1611–1620.

[45] R. Köferstein, F. Oehler, S.G. Ebbinghaus, Investigations of Nano-crystalline $Sr_{0.5}Ba_{0.5}Nb_2O_6$ and Bulk Ceramics Synthesized by a Polymerization Method Using PEG400, J. Eur. Ceram. Soc. 39 (2019) 1156–1163.

[46] R.M. Bozorth, E.F. Tilden, A.J. Williams, Anisotropy and Magnetostriction of Some Ferrites, Phys. Rev. 99 (1955) 1788–1798.

[47] K. Maaz, W. Khalid, A. Mumtaz, S.K. Hasanain, J. Liu, J.L. Duan, Magnetic characterization of $Co_{1-x}Ni_xFe_2O_4$ ($0 \le x \le 1$) Nanoparticles Prepared by Co-precipitation Route, Physica E41 (2009) 593–599.

[48] B. Liu, J. Ding, J. Yi, J. Yin, Magnetic Anisotropies in Cobalt-Nickel Ferrites ($NixCo_{1-x}Fe_2O_4$), J. Korean Phys. Soc. 52 (2008) 1483–1486.

[49] I. Aaeger, A.H. Morrish, B.M. Wanklyn, Magnetization Studies in Transition-Metal Niobates: I. $NiNb_2O_6$, Phys. Rev. B 15 (1977) 1465–1476.

[50] W. Scharf, H. Weitzel, I. Yaeger, I. Maartense, B.M. Wanklyn, Magnetic Structures of $CoNb_2O_6$, J. Magn. Magn. Mater. 13 (1979) 121–124.

[51] G.A. Sawatzky, F. van der Woude, A.H. Morrish, Mössbauer Study of Several Ferrimagnetic Spinels, Phys. Rev. 187 (1969) 747–757.

[52] J.H. Cho, S. Cho, J.H. Lee, H. Palneedi, J.H. Lee, H.P. Kim, N.J. Lee, S. Tigunta, S. Pojprapai, S. Kim, J. Ryu, Y.S. Oh, S. Hong, W. Jo, Room-temperature Multiferroicity in $NiFe_2O_4$ and its Magnetoelectric Coupling Intensified Through Defect Engineering, J. Am. Ceram. Soc. 104 (2021) 6384–6392.

[53] M.W. Schafer, Preparation and Properties of Ferrospinels Containing Ni^{3+}, J. Appl. Phys. 33 (1962) 1210–1211.

[54] Y. Kalyana Lakshmi, S. Bharadwaj, S. Chanda, C. Venkata Koti Reddy, S. Pola, K. V. Siva Kumar, Iron Ion Non-Stoichiometry and its Effect on Structural, Magnetic and Dielectric Properties of Cobalt Ferrites Prepared Using Oxalate Precursor Method, Mater. Chem. Phys. 295 (2023) 127172.

[55] A.H. Morrish, The Physical Principles of Magnetism, R. E. Krieger Publishing Company Inc., Huntington, New York, 1980.

[56] S.A. Ali, M.A. Matin, M.A. Hakim, M.F. Islam, Effects of $CoFe_2O_4$ substitution on magnetic properties of $NiFe_2O_4$ spinel ferrite, IOP Conf. Ser.: Mater. Sci. Eng. 438 (2018) 012017.

[57] P.K. Chougule, S.S. Kumbhar, Y.D. Kolekar, C.H. Bhosale, Enhancement in Curie Temperature of Nickel Substituted Co–Mn Ferrite, J. Magn. Magn. Mater. 375 (2014) 181–186.

[58] A. Broese van Groenou, P.F. Bongers, A.L. Stuyts, Magnetism, microstructure and crystal chemistry of spinel ferrites, Mater. Sci. Eng. 3 (1969) 317–392.

[59] C.M. Srivastava, G. Srinivasan, N.G. Nanadikar, Exchange Constants in Spinel Ferrites, Phys. Rev. B19 (1979) 499–507.

[60] P.G. Bercoff-, H.R. Bertorello, Exchange Constants and Transfer Integrals of Spine1 Ferrites, J. Magn. Magn. Mater. 169 (1997) 314–322.

[61] C.M.B. Henderson, J.M. Charnock, D.A. Plant, Cation Occupancies in Mg, Co, Ni, Zn, Al Ferrite Spinels: A Multi-Element EXAFS Study, J. Phys.: Condens. Matter 19 (2007) 076214.

[62] R.D. Shannon, Revised Effective Ionic Radii and Systematic Studies of Interatomic Distances in Halides and Chalcogenides, Acta Cryst A32 (1976) 751–767.

[63] P. Sowjanya, N. Pavan Kumar, A. Chelvane, M.V. Ramana Reddy, Synthesis and Analysis of Low Field High Magnetostrictive Ni-Co Ferrite for Magneto-Electric Energy Harvesting Applications, Mater. Sci. Eng. B279 (2022) 115674.

[64] C.E. Ciomaga, M. Airimioaei, I. Turcan, A.V. Lukacs, S. Tascu, M. Grigoras, N. Lupu, J. Banys, L. Mitoseriu, Functional Properties of Percolative $CoFe_2O_4$-$PbTiO_3$ Composite Ceramics, J. Alloys Compd. 775 (2019) 90–99.

[65] J.A. Paulsen, C.C.H. Lo, J.E. Snyder, A.P. Ring, L.L. Jones, D.C. Jiles, Study of the Curie Temperature of Cobalt Ferrite Based Composites for Stress Sensor Applications, IEEE Trans Magnet 39 (2003) 3316–3318.

[66] ed. by K. Uchino, Relaxor Ferroelectric-based Ceramics, in: K. Uchino (Ed.), Advanced Piezoelectric Materials Science and Technology, Woodhead Publishing Limited, Cambridge, 2010, p. 111. ed. byet seqq.

[67] F. Oehler, H.T. Langhammer, S.G. Ebbinghaus, Preparation and Dielectric Properties of $CaTaO_2N$ and $SrNbO_2N$ Ceramics, J. Eur. Ceram. Soc. 37 (2017) 2129–2136.

[68] S. Mokhtari, H. Ahmadvand, M.J. Fesharaki, H. Papi, P. Kameli, H. Salamati, Complex Magnetoelectric Effect in Multiferroic Composites: The Case of PFN-PT/(Co,Ni)Fe_2O_4, J. Phys. D: Appl. Phys. 52 (2019) 505001.

[69] S.V. Suryanarayana, Magnetoelectric Intercation Phenomena in Materials, Bull. Mater. Sci. 17 (1994), 1295–1270.

[70] A. Aubert, V. Loyau, F. Mazaleyrat, M. LoBue, Investigation of Piezomagnetism in Nickel Ferrite, IEEE Trans. Magn. 57 (2021) 2501105.

[71] B.K. Bammannavar, L.R. Naik, R.B. Pujar, B.K. Chougule, Resistivity Dependent Magnetoelectric Characterization of $Ni_{0.2}Co_{0.8}Fe_2O_4$ + $Ba_{0.8}Pb_{0.2}Zr_{0.8}Ti_{0.2}O_3$ Composites, J. Alloys. Compd. 477 (2009) L4–L7.

[72] F. Wang, G. Zhang, H. Yang, M. Liu, Y. Yang, Low Temperature Sintering and Magnetoelectric Properties of Laminated $BaTiO_3$/$BiY_2Fe_5O_{12}$ Composites, J. Alloys Compd. 632 (2015) 460–466.

[73] S.D. Bhame, M.M. Shirolkar, P.A. Joy, Magnetic and Magnetoelastic Properties of Ni-Substituted Cobalt Ferrite, IEEE Magn. Lett. 12 (2021) 2504205.

[74] V.L. Mathe, A.D. Sheikh, Magnetostrictive Properties of Nanocrystalline Co–Ni Ferrites, Physica B 405 (2010) 3594–3598.
[75] A. Aubert, V. Loyau, Y. Pascal, F. Mazaleyrat, M. LoBue, Dynamic Magnetostriction of $CoFe_2O_4$ and Its Role in Magnetoelectric Composites, Phys. Rev. Appl. 9 (2018) 044035.
[76] C.W. Nan, Magnetoelectric Effect in Composites of Piezoelectric and Piezomagnetic Phases, Phys. Rev. B 50 (1994) 6082–6088.
[77] M. Fiebig, Revival of the Magnetoelectric Effect, J. Phys. D: Appl. Phys. 38 (2005) R123–R152.
[78] R.V. Coates, H.F. Kay, Dielectric Properties of Some Metaniobate and Metatantalate Ceramics, Philos. Mag. 36 (1958) 1449–1459.

Supporting Information

Magnetoelectric, dielectric, and magnetic investigations of multiferroic $Ni_xCo_{1-x}Fe_2O_4$–$Sr_yBa_{1-y}Nb_2O_6$ composites

Roberto Köferstein*, Maria-Sophie Wartmann, and Stefan G. Ebbinghaus

Institute of Chemistry, Martin Luther University Halle-Wittenberg,

Kurt-Mothes-Straße 2, 06120 Halle, Germany.

* Corresponding author

Tel.: +49-345-5525630; Fax: +49-345-5527028.

E-mail address: roberto.koeferstein@chemie.uni-halle.de

Table 1: Theoretical bulk densities of $(NiFe_2O_4)_{0.3}$–$(Sr_yBa_{1-y}Nb_2O_6)_{0.7}$ composites			
Composites $(NiFe_2O_4)_{0.3}$–$(Sr_yBa_{1-y}Nb_2O_6)_{0.7}$	Single crystal densities of the single composite compounds (g cm^{-3})		Calculated theoretical bulk densities of the composites according to [2]* (g cm^{-3})
	$Sr_yBa_{1-y}Nb_2O_6$	$NiFe_2O_4$ [1]	
y = 0.3	5.40[a]	5.38	5.39
y = 0.5	5.37[b]	5.38	5.37
y = 0.6	5.28[c]	5.38	5.30
y = 0.7	5.28[d]	5.38	5.30

[1] M. A. Gabal and Y. M. Al Angari, Mater. Chem. Phys. 118 (2009)153–160; ICSD #165448)
[2] G. W. Marks and L. A. Monson, Ind. Eng. Chem. 47 (1955) 1611–1620.
* The theoretical bulk densities represent the maximum achievable densities.

The used X-ray densities were taken from available database entries near to the sample composition.
a) $Sr_{0.33}Ba_{0.67}Nb_2O_6$ (S. Podlozhenov, et al., Acta Cryst. B 62 (2006) 960–965; ICSD #240387)
b) $Sr_{0.50}Ba_{0.50}Nb_2O_6$ (S. S. Rathore and S. Vitta, AIP Conf. Proc. 1591 (2014) 133–135; ICSD #291175)
c) $Sr_{0.61}Ba_{0.39}Nb_2O_6$ (S. Podlozhenov, et al., Acta Cryst. B 62 (2006) 960–965; ICSD #240389)
d) $Sr_{0.75}Ba_{0.27}Nb_2O_6$ (P. B. Jamieson, et al., J. Chem. Phys. 48 (1968) 5048–5047; ICSD #15614)

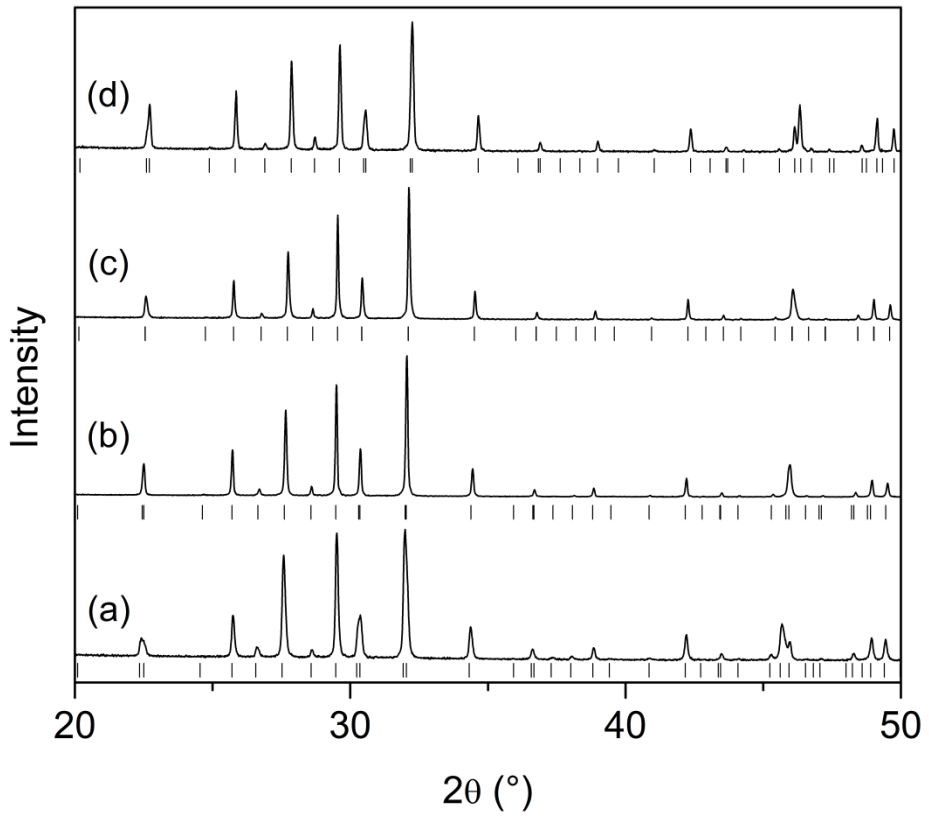

Fig. S1: Room-temperature XRD patterns of (a) $Sr_{0.3}Ba_{0.7}Nb_2O_6$, calcined at 1473 K for 5 h, b) $Sr_{0.5}Ba_{0.5}Nb_2O_6$, calcined at 1473 K for 5 h, (c) $Sr_{0.6}Ba_{0.4}Nb_2O_6$, calcined at 1573 K for 5 h and (d) $Sr_{0.7}Ba_{0.3}Nb_2O_6$, calcined at 1703 K for 30 h; (heating-/cooling rate 5 K min^{-1}). The vertical bars show peak positions according to the available database entries close to the sample composition: (a) ICSD #240387 ($Sr_{0.33}Ba_{0.67}Nb_2O_6$), (b) ICSD #240388 ($Sr_{0.48}Ba_{0.52}Nb_2O_6$), (c) ICSD #240389 ($Sr_{0.61}Ba_{0.39}Nb_2O_6$) (d) ICSD #15614 ($Sr_{0.75}Ba_{0.27}Nb_2O_6$).

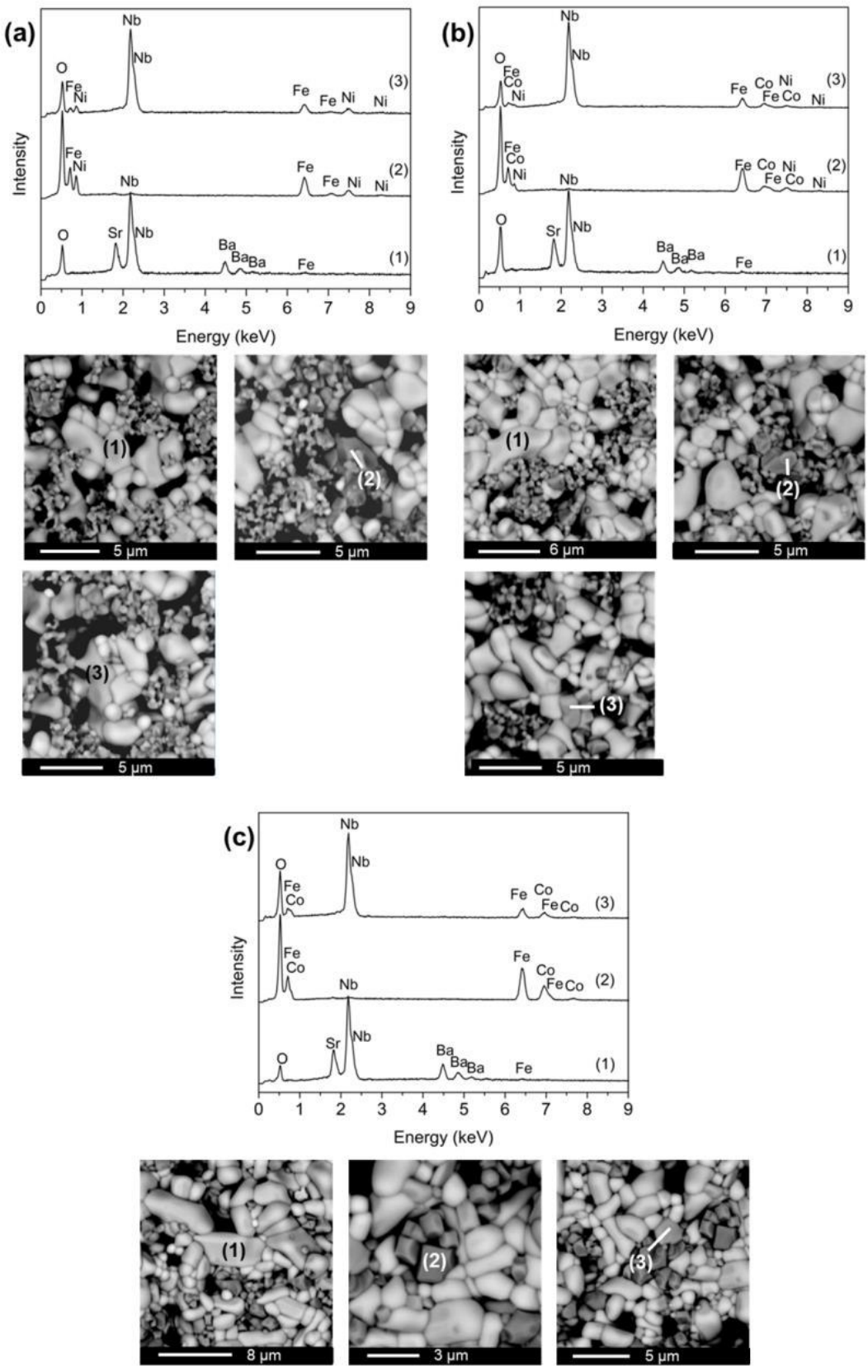

Fig. S2: EDX spectra of selected $(Ni_xCo_{1-x}Fe_2O_4)_{0.3}$–$(Sr_{0.5}Ba_{0.5}Nb_2O_6)_{0.7}$ composite ceramics sintered at 1373 K for 1 h with (a) $x = 1$, (b) $x = 0.5$, and (c) $x = 0$ at the positions marked in the pictures below. (1) $Sr_{0.5}Ba_{0.5}Nb_2O_6$ grain, (2) $Ni_xCo_{1-x}Fe_2O_4$ grain, and (3) grain of the secondary phase (MFe_2O_6, M = Ni/Co).

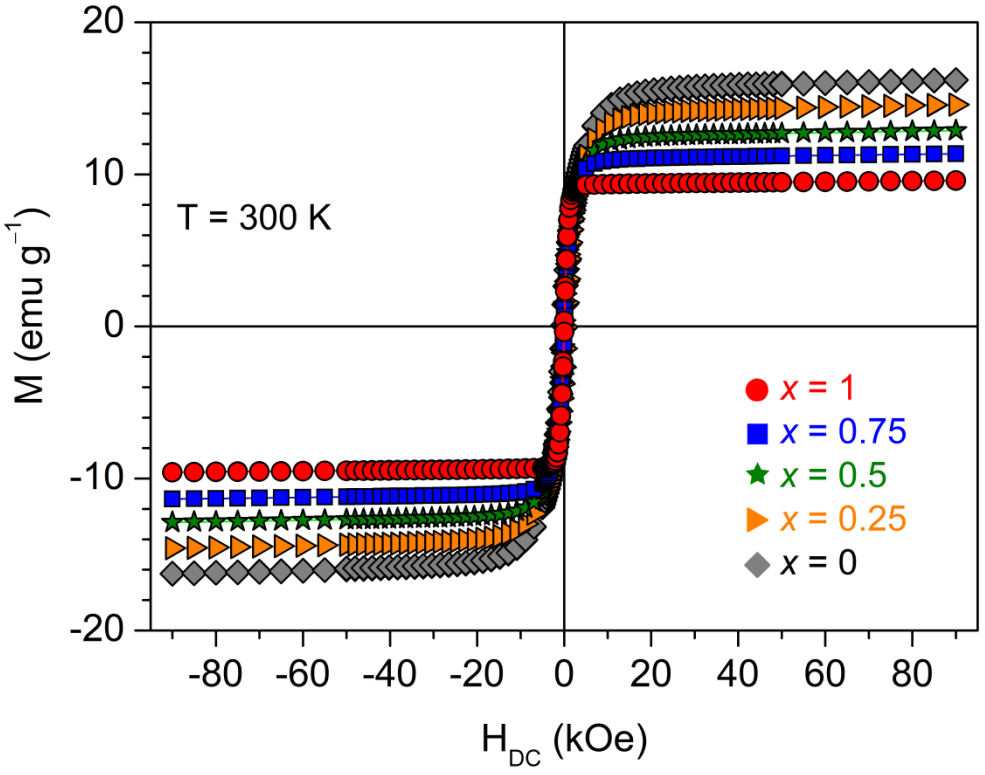

Fig. S3: Magnetization at 300 K for $(Ni_xCo_{1-x}Fe_2O_4)_{0.3}$–$(Sr_{0.5}Ba_{0.5}Nb_2O_6)_{0.7}$ composite ceramics sintered at 1373 K for 1 h. The magnetization values are given with respect to the sample mass.

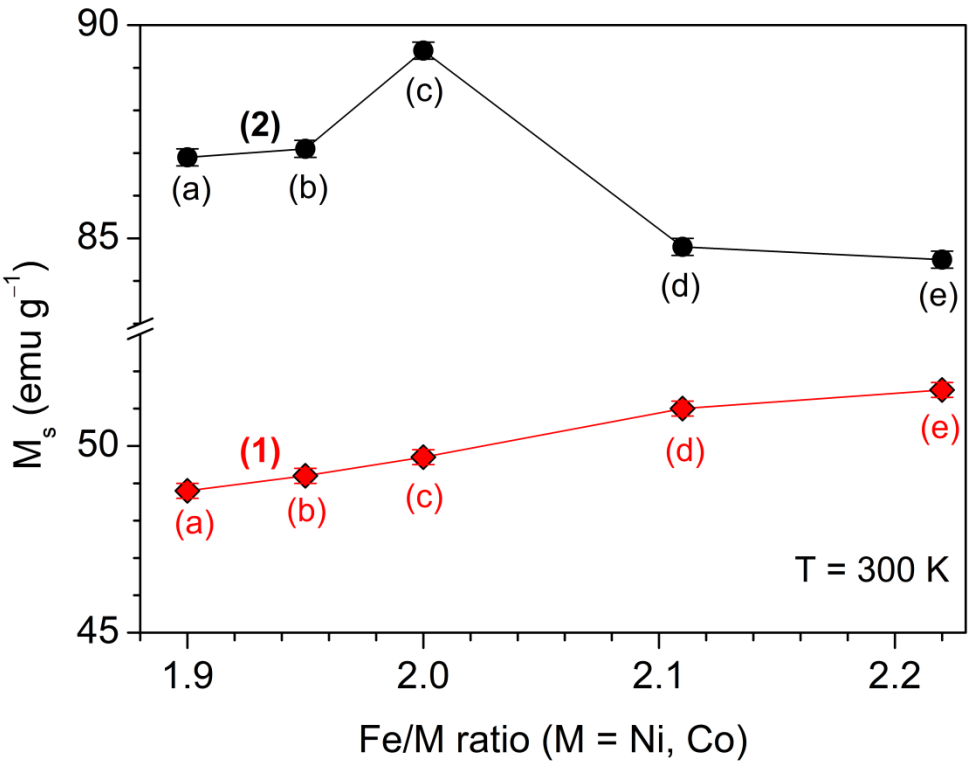

Fig. S4: Saturation magnetization (Ms) depending on the Fe/M ratio in $NiFe_2O_4$ (**1**) and $CoFe_2O_4$ (**2**) ceramics sintered at 1373 K for 1 h. a) $MFe_{1.9}O_{3.85}$, b) $MFe_{1.95}O_{3.93}$, c) MFe_2O_4, d) $M_{0.95}Fe_2O_{3.95}$, e) $M_{0.90}Fe_2O_{3.9}$ (M = Ni, Co).

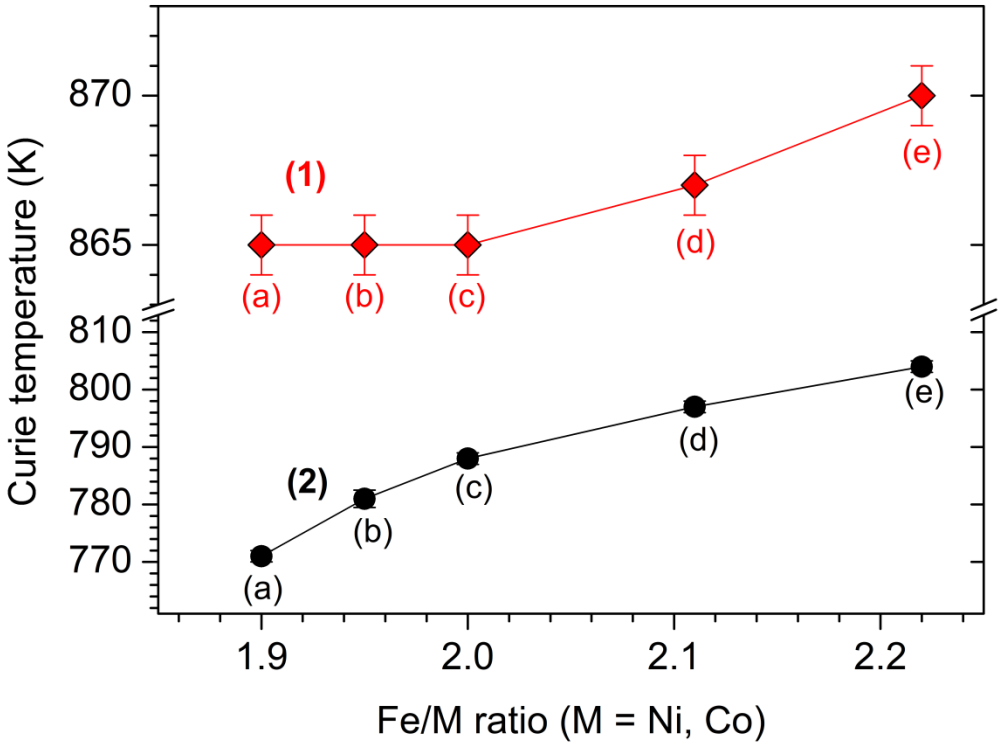

Fig. S5: Curie temperature of $NiFe_2O_4$ (**1**) and $CoFe_2O_4$ (**2**) ceramics sintered at 1373 K for 1 h with different Fe/M ratios. a) $MFe_{1.9}O_{3.85}$, b) $MFe_{1.95}O_{3.93}$, c) MFe_2O_4, d) $M_{0.95}Fe_2O_{3.95}$, e) $M_{0.90}Fe_2O_{3.9}$ (M = Ni, Co). The Curie temperatures were determined by thermogravimetric measurements in a magnetic field from the cooling curve.

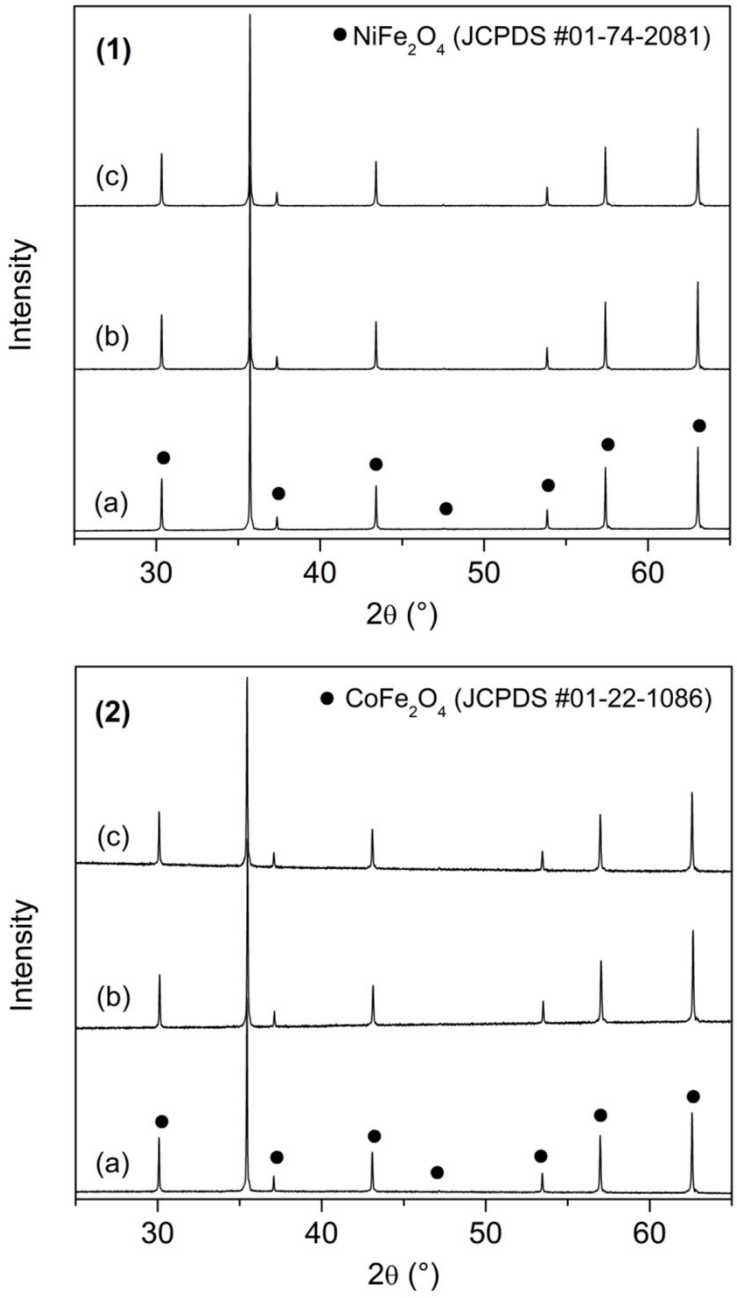

Fig. S6: Room-temperature XRD patterns of $NiFe_2O_4$ (**1**) and $CoFe_2O_4$ (**2**) ceramics sintered at 1373 K for 1 h with different Fe/M ratios (M = Ni, Co). a) $MFe_{1.9}O_{3.85}$ (Fe/M = 1.90), b) MFe_2O_4 (Fe/M = 2.00), c) $M_{0.90}Fe_2O_{3.9}$ (Fe/M = 2.22). The patterns were recorded with a prolonged counting time of 5 s per data point.

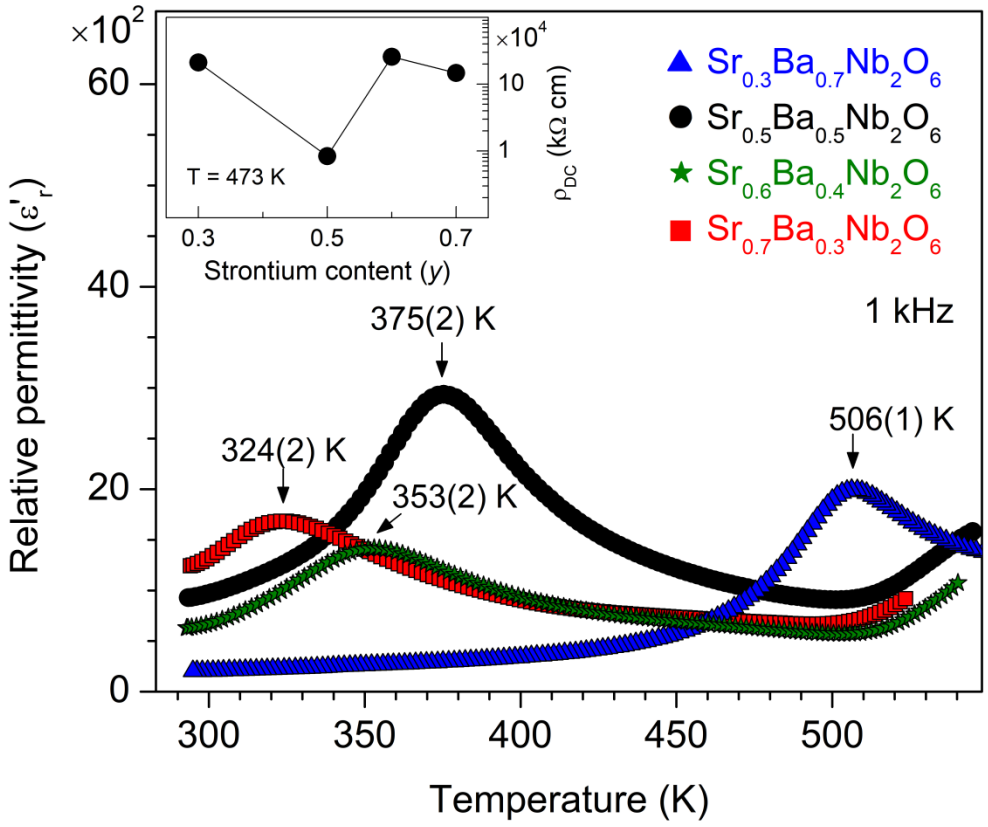

Fig. S7: Dependence of the real part of the permittivity (ε_r') on temperature at 1 kHz for various $Sr_yBa_{1-y}Nb_2O_6$ ceramic bodies sintered between 1473 and 1703 K for 1 h. For the sake of clarity every second data point is represented by a symbol. The inset shows the specific DC resistivity (ρ_{DC}) depending in the strontium content (y) of the $Sr_yBa_{1-y}Nb_2O_6$ ceramics. The DC resistivity values were calculated by fitting the impedance data by an equivalent circuit consisting of one resistance-capacitor (RC) element including a constant phase-shift element. The uncertainties of the data are smaller than the symbol size.

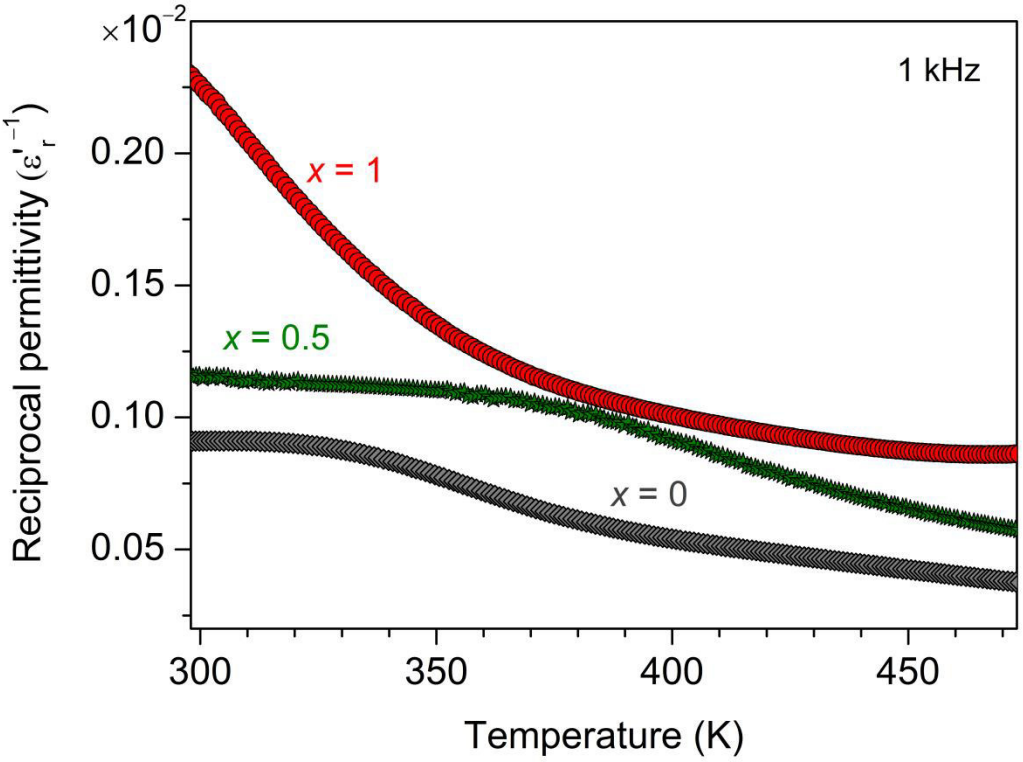

Fig. S8: Reciprocal real part of the permittivity ($\varepsilon_r'^{-1}$) versus temperature at 1 kHz of $(Ni_xCo_{1-x}Fe_2O_4)_{0.3}$–$(Sr_{0.5}Ba_{0.5}Nb_2O_6)_{0.7}$ ceramic bodies sintered for 1 h at 1373 K.

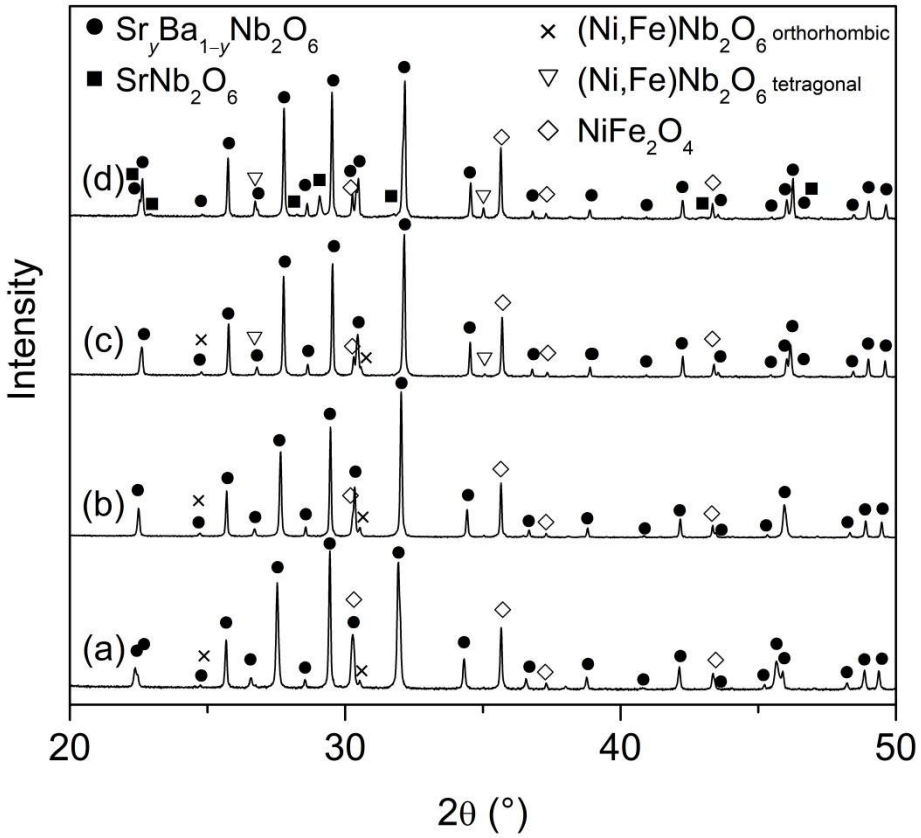

Fig. S9: Room-temperature XRD patterns of $(NiFe_2O_4)_{0.3}$–$(Sr_yBa_{1-y}Nb_2O_6)_{0.7}$ crushed composite ceramics after sintering at 1373 K for 1 h (heating-/cooling rate 5 K min^{-1}).

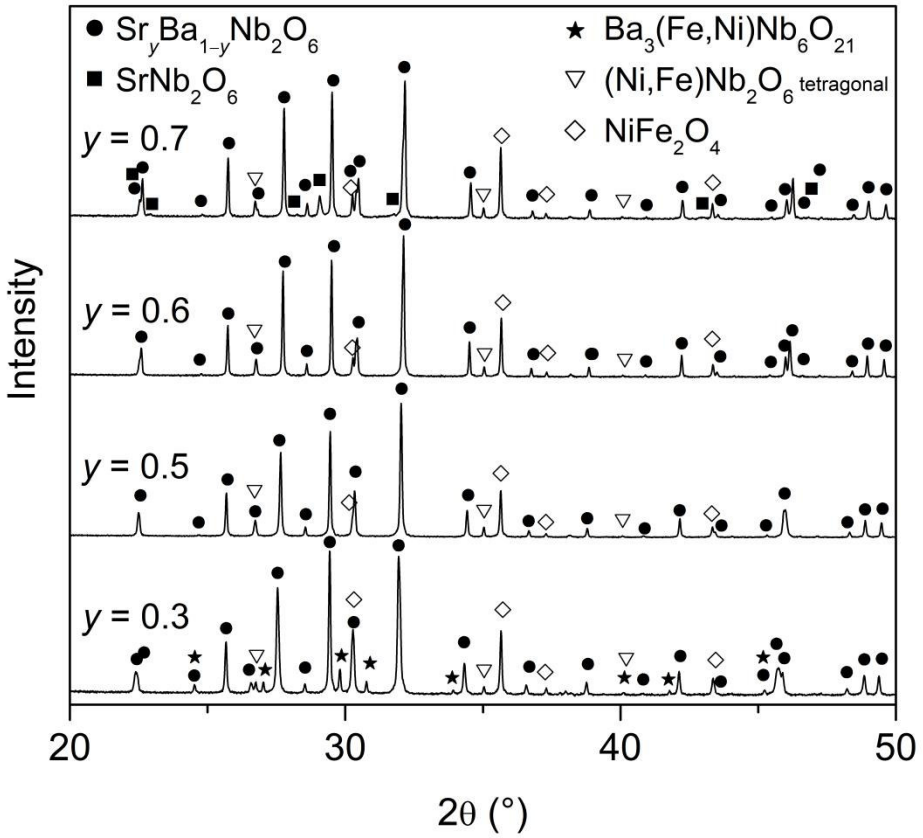

Fig. S10: Room-temperature XRD patterns of $(NiFe_2O_4)_{0.3}$–$(Sr_yBa_{1-y}Nb_2O_6)_{0.7}$ crushed composite ceramics after sintering at 1423 K for 1 h (heating-/cooling rate 5 K min^{-1}). For the sample with $y = 0.3$, EDX measurements of $Ba_3(Fe,Ni)Nb_2O_{21}$ grains suggest a Fe/Ni ratio of about 2.

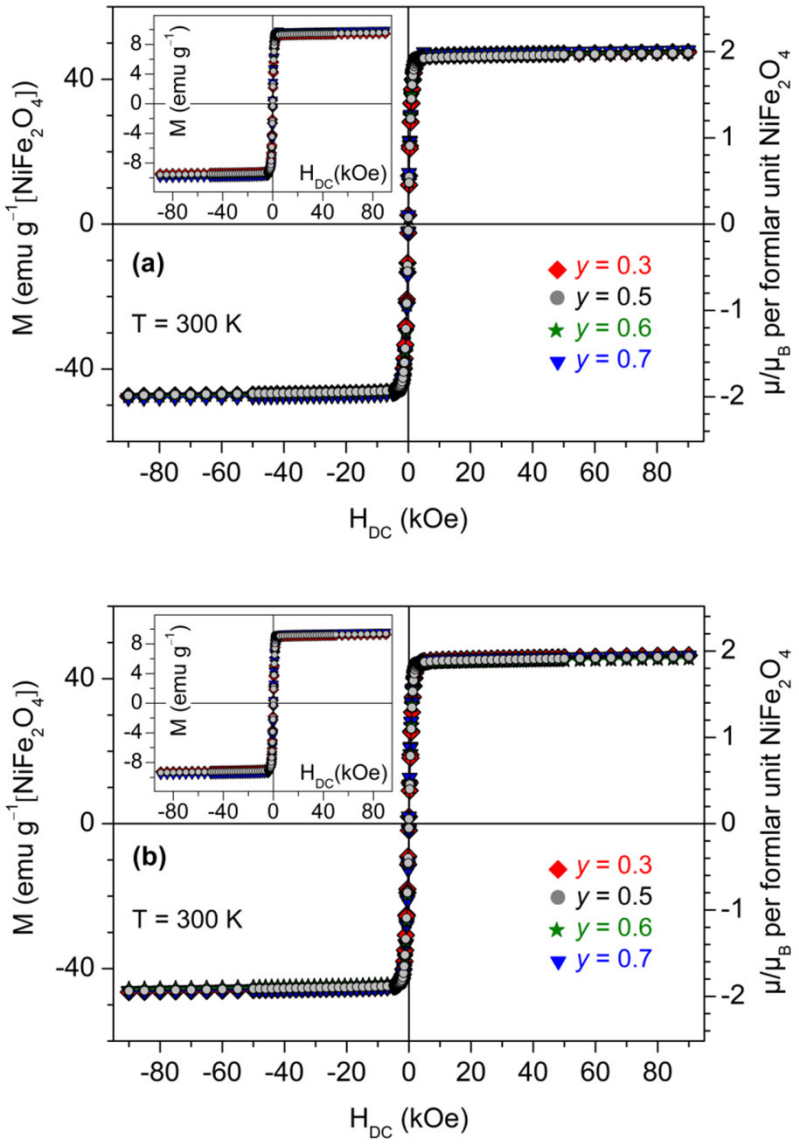

Fig. S11: Magnetization at 300 K for $(NiFe_2O_4)_{0.3}$–$(Sr_yBa_{1-y}Nb_2O_6)_{0.7}$ composite ceramics sintered at 1373 K (a) and 1423 K (b) for 1 h. The magnetization values are given with respect to the nominal $NiFe_2O_4$ content. In the inset the magnetization values are given with respect to the sample mass.

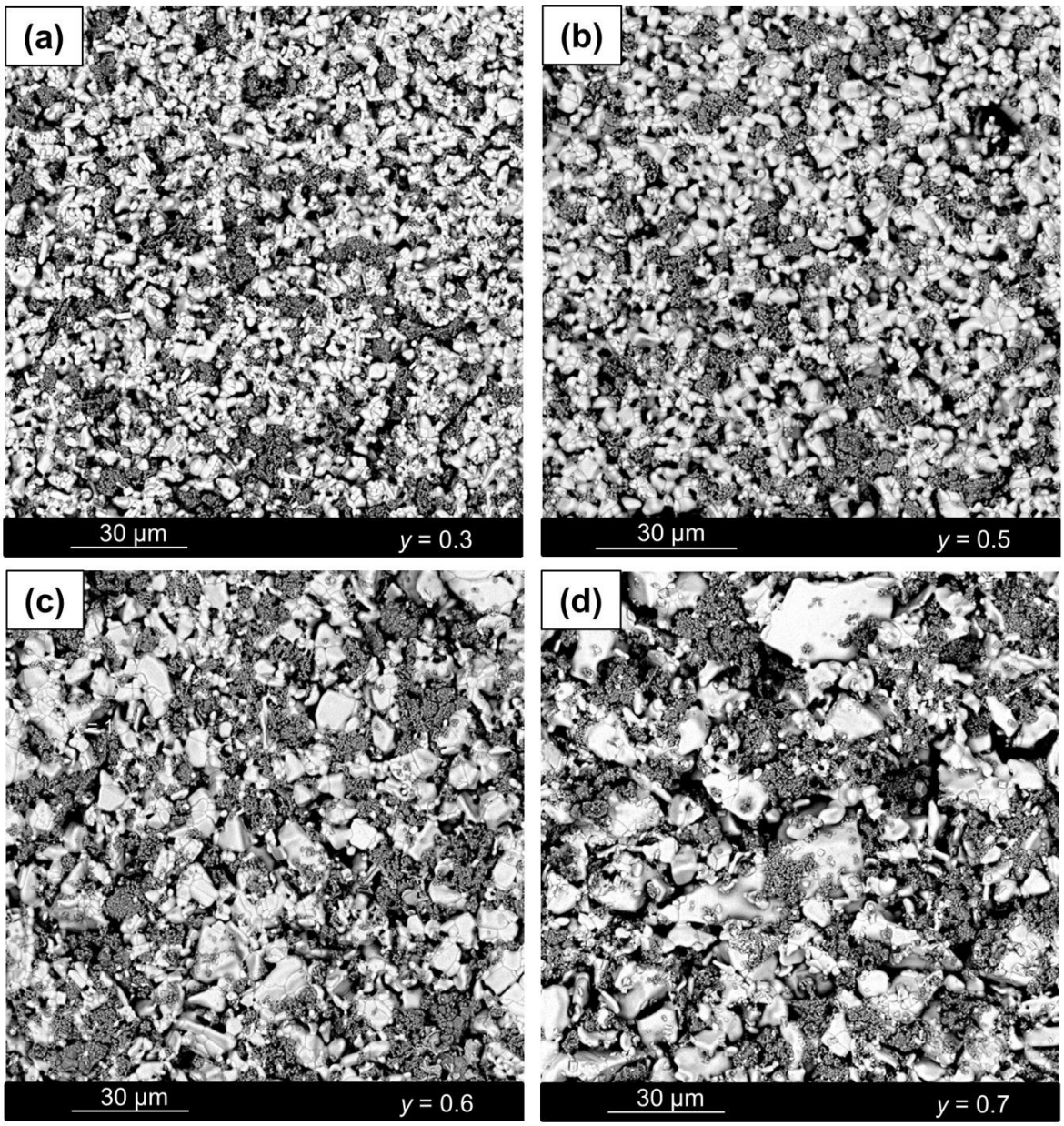

Fig. S12: SEM-BSE images of $(NiFe_2O_4)_{0.3}$–$(Sr_yBa_{1-y}Nb_2O_6)_{0.7}$ ceramics sintered at 1373 K for 1 h.

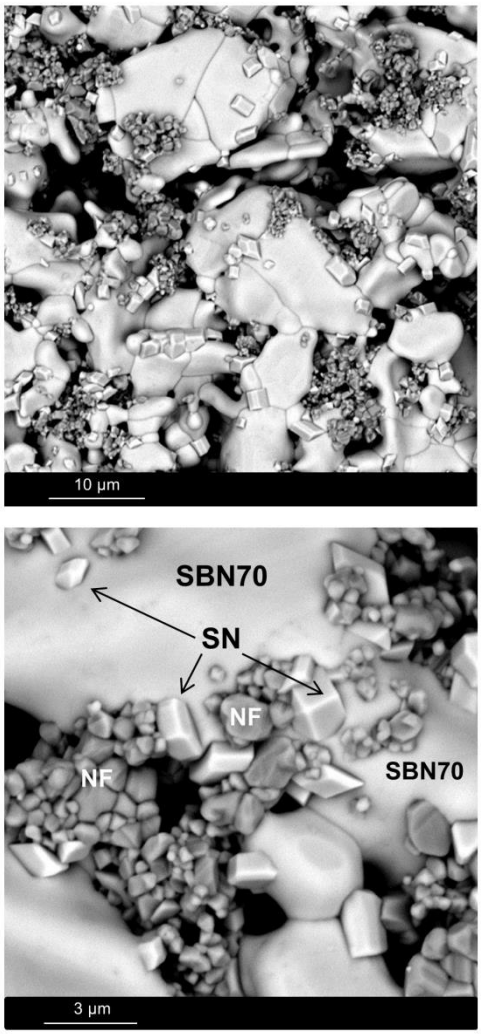

Fig. S13: SEM-BSE images of $(NiFe_2O_4)_{0.3}$–$(Sr_{0.7}Ba_{0.3}Nb_2O_6)_{0.7}$ ceramics sintered at 1373 K for 1 h. SBN70 = $Sr_{0.7}Ba_{0.3}Nb_2O_6$, SN = $SrNb_2O_6$, NF = $NiFe_2O_4$.

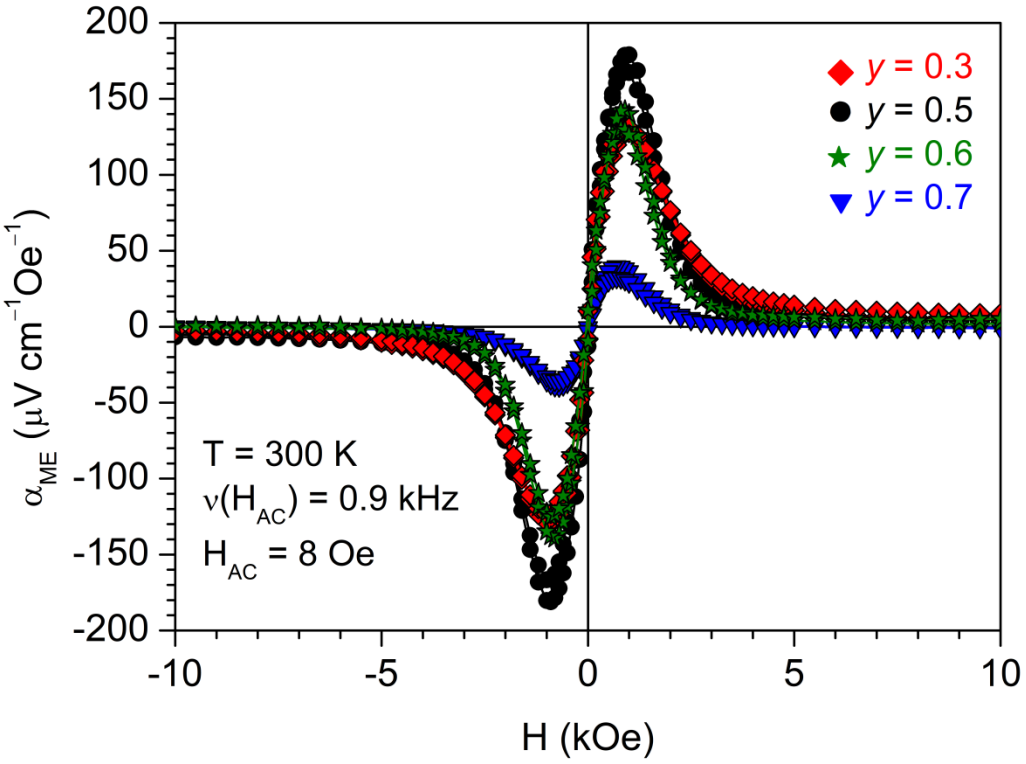

Fig. S14: Magnetoelectric coefficient (α_{ME}) vs. magnetic DC field for $(NiFe_2O_4)_{0.3}$–$(Sr_yBa_{1-y}Nb_2O_6)_{0.7}$ composites sintered at 1373 K for 1 h.